

# Multifractal Analysis of the Interstellar Medium. First application to Hi-GAL Observations

Davide Elia,<sup>1\*</sup> Francesco Strafella,<sup>2,3</sup> Sami Dib,<sup>4,5</sup> Nicola Schneider,<sup>6</sup> Patrick Hennebelle,<sup>7,8,9</sup> Stefano Pezzuto,<sup>1</sup> Sergio Molinari,<sup>1</sup> Eugenio Schisano,<sup>1</sup> Sarah E. Jaffa<sup>10</sup>

<sup>1</sup>*Istituto di Astrofisica e Planetologia Spaziali, INAF, Via Fosso del Cavaliere 100, Roma, 00133, Italy*

<sup>2</sup>*Dipartimento di Matematica e Fisica ‘Ennio De Giorgi’, Università del Salento, CP 193, I-73100 Lecce, Italy*

<sup>3</sup>*INFN Sezione di Lecce, CP 193, I-73100 Lecce, Italy*

<sup>4</sup>*Niels Bohr International Academy, Niels Bohr Institute, Blegdamsvej 17, DK-2100, Copenhagen, Denmark*

<sup>5</sup>*Max-Planck Institute für Astronomie, Königstuhl 17, 69117, Heidelberg, Germany*

<sup>6</sup>*I. Physik. Institut, University of Cologne, D-50937 Cologne, Germany*

<sup>7</sup>*IRFU, CEA, Université Paris-Saclay, 91191 Gif-sur-Yvette, France*

<sup>8</sup>*Université Paris Diderot, AIM, Sorbonne Paris Cité, CEA, CNRS, 91191 Gif-sur-Yvette, France*

<sup>9</sup>*LERMA (UMR CNRS 8112), Ecole Normale Supérieure, 75231 Paris Cedex, France*

<sup>10</sup>*School of Physics and Astronomy, Cardiff University, Cardiff CF24 3AA, Wales, UK 0000-0002-6711-6345*

Accepted XXX. Received YYY; in original form ZZZ

## ABSTRACT

The multifractal geometry remains an under-exploited approach to describe and quantify the large-scale structure of interstellar clouds. In this paper, the typical tools of multifractal analysis are applied to *Herschel* far-infrared (70–500  $\mu\text{m}$ ) dust continuum maps, which represent an ideal case of study. This dust component is a relatively optically thin tracer at these wavelengths and the size in pixel of the maps is well suitable for this statistical analysis. We investigate the so-called multifractal spectrum and generalised fractal dimension of six Hi-GAL regions in the third Galactic quadrant. We measure systematic variations of the spectrum at increasing wavelength, which generally correspond to an increasing complexity of the image, and we observe peculiar behaviours of the investigated fields, strictly related to the presence of high-emission regions, which in turn are connected to star formation activity. The same analysis is applied to synthetic column density maps, generated from numerical turbulent molecular cloud models and from fractal Brownian motion (fBm), allowing for the confrontation of the observations with models with well controlled physical parameters. This comparison shows that, in terms of multifractal descriptors of the structure, fBm images exhibit a very different, quite unrealistic behaviour when compared with Hi-GAL observations, whereas the numerical simulations appear in some cases (depending on the specific model) more similar to the observations. Finally, the link between mono-fractal parameters (commonly found in the literature) and multifractal indicators is investigated: the former appear to be only partially connected with the latter, with the multifractal analysis offering a more extended and complete characterization of the cloud structure.

**Key words:** ISM: clouds – ISM: structure – Infrared: ISM – stars: formation – methods: statistical – techniques: image processing

## 1 INTRODUCTION

The complex morphology of Galactic interstellar clouds generally eludes a description simply based on the typical shapes of Euclidean geometry (e.g., Scalo 1990; Elmegreen & Falgarone 1996; Pfenninger 1996). The mostly self-similar appearance of the interstellar medium (ISM), especially at scales  $L \gtrsim 1$  pc is generally thought

to be the result of turbulence (Elmegreen 1995; Elmegreen & Scalo 2004; Dib & Burkert 2005; Krumholz 2014), because of the intrinsic self-similarity of this phenomenon, triggered by the very high value of the Reynolds number in these environments. The fractal geometry is largely invoked to provide a quantitative characterization of the ISM morphology, as it can be deduced from far-infrared (FIR) or sub-millimetre maps, through fractal descriptors (Stutzki et al. 1998; Bensch et al. 2001; Schneider et al. 2011; Sun et al. 2018; Elia et al. 2014, hereafter Paper I) and comparing these quantities with

\* E-mail: davide.elia@iaps.inaf.it

theoretical expectations has two important advantages. On the one hand, a comparison between models and observations gives indications about the kind of turbulence that is prevalent in the observed cloud and, on the other hand, the obtained fractal parameters can be used as further constraints for future simulations. In this respect, fractal or, in a broad sense, statistical analysis techniques are applied also to numerical simulations of turbulent clouds, to make possible a comparison between model and ISM morphological properties. Three-dimensional magneto-hydrodynamic simulations have been characterised in terms of probability density function, structure function and power spectrum (Kowal et al. 2007; Kritsuk et al. 2007), fractal dimension (Federrath et al. 2009), or dendrograms (Burkhart et al. 2013).

It should also be emphasised that natural fractal structures, such as ISM, are self-similar only in a statistical sense (*stochastic fractals*) and show complexity only over a finite range of scales. Identifying such a range, which should correspond to the scales actually involved by the turbulent energy cascade, can give important information on the injection and dissipation scale of turbulence (see Paper I, and references therein). Interestingly, the latter is expected to correspond to the characteristic size of gravity-dominated structures (filaments and cores) relevant for star formation, as highlighted, e.g., by Falgarone et al. (2004) and Schneider et al. (2011) (for more recent analysis of the turbulence-regulated star formation, see also Burkhart et al. 2017; Mocz et al. 2017).

This (mono-)fractal approach, however, still underlies a certain degree of degeneracy: as said above, a large number of natural objects exhibit properties of self-similarity, but can not be described as perfect fractals, especially because such a description is based on a sole parameter, namely the fractal dimension. In contrast, *Multifractal geometry* provides a more suited mathematical framework for detecting and identifying complex local structure, and for describing local singularities. It is invoked in the fields of economy, medicine, hydrography, environmental sciences, and physics (e.g. in studying turbulent flows). In astrophysics, it has been used, for example, in the study of the distribution of galaxies (Mandelbrot 1989; Borgani et al. 1993; Pan & Coles 2000; de La Fuente Marcos & de La Fuente Marcos 2006), gamma-ray burst time series (Meredith et al. 1995), and solar activity (Wu et al. 2015; Cadavid et al. 2016; Maruyama et al. 2017).

The first application of the multifractal approach to characterize the ISM structure was carried out by Chappell & Scalo (2001), who analyzed 13 *IRAS* maps (at 60 and 100  $\mu\text{m}$ ) taken from Chamaeleon-Musca, R Corona Australis and Scorpius-Ophiucus star forming regions, all located at distance  $d < 160$  pc from the Sun, but spanning a relatively wide range of different conditions of star formation. A multifractal behaviour of the investigated clouds was revealed over the range 0.4-4 pc, and a possible relation with underlying turbulent cascades and hierarchical structure was found. While the multifractal properties of a cloud can be directly related to its geometry, a direct relation with the properties of the star formation is not found by these authors; this link has been established indirectly for the first time by Tassis (2007) using global parameters of external galaxies. Finally, Khalil et al. (2006) studied the multifractal structure of Galactic atomic hydrogen through wavelet transform techniques, discussing arm vs inter-arm differences.

As already pointed out in Paper I, the advent of *Herschel* (Pilbratt et al. 2010) offered an extraordinary chance for studying the morphology of the cold Galactic ISM, thanks to the combination of several favourable conditions and features: *i*) the spectral coverage of *Herschel* photometric surveys (70 – 500  $\mu\text{m}$ ) encompasses the peak of the continuum emission of cold dust ( $T \leq 50$  K), with

the dust getting optically thinner at increasing wavelengths, which helps revealing the structure of dense clouds with unprecedented accuracy; *ii*) the angular resolution of *Herschel* photometric observations ( $6'' - 36''$ ) is better or comparable with that of the most recent CO surveys of the ISM (e.g., Jackson et al. 2006; Burton et al. 2013; Schuller et al. 2017), and their dynamic range is so large (more than two orders of magnitude, e.g., Molinari et al. 2016) that the obtained 2-D picture of the ISM structure generally turns out to be highly detailed and reliable; *iii*) large *Herschel* photometric surveys produced a huge amount of data, corresponding to a wide variety of Galactic locations, physical conditions, and star formation modes to be compared; *iv*) thanks to good angular resolution and excellent mapping capabilities, single *Herschel* maps represent highly suitable data sets for pixel statistical analysis, namely techniques aimed at deriving fractal properties of maps starting from intensity values in single pixels. This improvement can be appreciated, for instance, by comparing how much the size in pixels of the analysed maps increased from the pioneering work of, e.g., Stutzki et al. (1998) (several tens or a few hundred pixels) to that of Paper I (up to a few thousands of pixels).

Despite this potential, the promising approach of Chappell & Scalo (2001) for describing the structure of the ISM through multifractal parameters has not been yet applied to *Herschel* maps. With this paper we intend to fill this gap. Furthermore, choosing the same fields already analysed through mono-fractal descriptors in Paper I, we explore possible relations between mono- and multifractal parameters for any investigated field. Finally, analysing with the same techniques also column density maps obtained from numerical simulations of interstellar turbulence, we search for possible recipes connecting the quantitative description provided by multifractal tools and the underlying physics of the analysed regions.

The paper is organized as follows: in Section 2 the analysed maps, both observational and synthetic, are presented. In Section 3 basics of multifractal geometry are introduced, together with a description of the tools used in the rest of the paper. In Section 4 the results of the multifractal analysis of the aforementioned data sets are reported and discussed by means of specific diagnostics, while our conclusions are given in Section 5. Additional details and discussion of the method are reported in the Appendices A, B, and C.

## 2 ANALYSED FIELDS

### 2.1 Hi-GAL maps

The observational sets chosen for this analysis are six  $1.5^\circ \times 1.5^\circ$  fields extracted from the Hi-GAL programme (Molinari et al. 2010), the photometric survey of the entire Galactic plane carried out at the 70, 160, 250, 350, and 500  $\mu\text{m}$  wavelengths with the two cameras PACS (Poglitsch et al. 2010) and SPIRE (Griffin et al. 2010). The original  $\sim 2.2^\circ \times 2.2^\circ$  Hi-GAL tiles obtained in the five aforementioned bands have a nominal resolution<sup>1</sup> of 5.6'', 11.3'', 17.6'', 23.9'', and 35.1'', and a pixel size of 3.2'', 4.5'', 6'', 8'', and 11.5'', respectively (Molinari et al. 2016).

The fields were chosen in the third Galactic quadrant (Elia et al. 2013): the central four, designated as  $\ell 217$ ,  $\ell 220$ ,  $\ell 222$ ,  $\ell 224$

<sup>1</sup> Actually, due to the PACS data co-adding on-board *Herschel*, the resulting point-spread functions are elongated along the scan direction, with a measured size of  $5.8'' \times 12.1''$  at 70  $\mu\text{m}$ , and  $11.4'' \times 13.4''$  at 160  $\mu\text{m}$ , respectively (Lutz 2012).

**Table 1.** Geometric properties of analysed frames.

Map type	Frame size pixel	$N_{\text{divisors}}$	Frame angular size "
70 $\mu\text{m}$	1690	10	5408
160 $\mu\text{m}$	1200	28	5400
250 $\mu\text{m}$	900	25	5400
350 $\mu\text{m}$	675	10	5400
500 $\mu\text{m}$	470	6	5405
fBm	1000	14	...
Mod.: Solenoidal	256	7	...
Mod.: Compressive	256	7	...
Mod.: Hydrodynamical	2048	10	...
Mod.: High-magnetization	2048	10	...

(from the original names of Hi-GAL the tiles they were extracted from), respectively, are already described (including data reduction and map making details) in Elia et al. (2013) and in Paper I. These fields were selected based on the following considerations:

(i) Ideally, each selected field should contain emission from a single Galactic component, i.e. from dust distributed within a limited range of heliocentric distances. In this portion of the Galactic plane, NANTEN data (Onishi et al. 2005; Elia et al. 2013) show a simple structure of the velocity field (Paper I, their Figure 1), so that each of the chosen Hi-GAL fields can be associated with a single predominant velocity component, i.e. a single coherent cloud.

(ii) The clipping of original tiles must be performed on the area observed by both PACS and SPIRE, choosing the same box for all the five bands, in order to analyse the same area of the sky at all wavelengths, in the limit of pixelation.

(iii) The clipped maps are chosen to be square-shaped and must be as large as possible, in order to increase the statistical relevance of the results and expand the range of spatial scales that are probed.

In addition to these requirements, for this work we also impose that

(iv) The size of the analysed maps must be a number of pixels characterised by a large enough number of integer factors, for the reasons that will be explained in Section 3.3.

About cropping the maps, it is difficult to find a common angular size, for all the five bands, which contextually corresponds to sizes (in pixels) satisfying the aforementioned property. For this reason we slightly adjusted the number of pixels composing the maps at each band, finding a final set of frame sizes in pixels approximately corresponding to  $1.5^\circ$  (depending on the wavelength, see Table 1). As a consequence, the maps analysed in this work turn out to be slightly smaller than those for which the fractal dimension was derived in Paper I, making it necessary to re-compute it (see Appendix C) in view of a comparison with multi-fractal properties (Section 4.3).

In Table 1 we report for each band the size of the maps in pixels, and the corresponding number of factors<sup>2</sup> and angular scale in arcseconds.

Furthermore, we include the two Hi-GAL tiles  $\ell 215$  and  $\ell 226$  that extend the sample to the West and to the East, respectively. In total, we have six tiles in five bands plus column density maps, i.e.

<sup>2</sup> For example, at 350  $\mu\text{m}$  the chosen map size is  $675 \times 675$  pixels. Except for 1 and itself, the side 675 has the following integer divisors: 3, 5, 9, 15, 25, 27, 45, 75, 135, 225, which therefore allow to perfectly cover the map with 10 possible box grids, and so on.

a total of 36 maps analysed in this work. All maps are displayed in Figure 1.

In Elia et al. (2013) an analysis of the gas velocity field, as derived from NANTEN CO(1-0) spectral line observations, was carried out for the four central tiles. It highlighted a prominence of emission from a closer component (at distances around  $\langle d \rangle_{\text{I}} = 1.1$  kpc) for the two Eastern tiles  $\ell 224$  and  $\ell 222$ , and from a farther component (around  $\langle d \rangle_{\text{II}} = 2.2$  kpc) for the two Western ones,  $\ell 220$  and  $\ell 217$ . These two components are also spatially segregated, since their reciprocal contamination degree is very low in the NANTEN data. Moreover, the contamination from two further and fainter velocity components ( $\langle d \rangle_{\text{III}} = 3.3$  kpc,  $\langle d \rangle_{\text{IV}} = 5.8$  kpc), is negligible in turn, even more after appropriate map cropping (see Figure 1). In the four central panels of the second row in Figure 1 the low degree of contamination for the four corresponding Hi-GAL fields can be appreciated. This made it possible, in Paper I, to associate each tile to only one of the two main velocity components of the region. In this paper, with the additional  $\ell 215$  and  $\ell 226$  tiles, we extend the basic analysis of the velocity field to these tiles. Looking at CO intensity contours obtained separately for each of the four aforementioned Galactic components, and overplotted on Hi-GAL 160  $\mu\text{m}$  maps (Figure 1, second row, the leftmost and rightmost tile, respectively), one can see how the region in  $\ell 226$  is dominated by component I, whereas the one in  $\ell 215$  is dominated by component II, so that, in conclusion, we can associate the three Eastern tiles to component I, and the three Western ones to component II, respectively.

## 2.2 Turbulent ISM simulations

We compare the observational data to the density structures found in 3-dimensional numerical simulations provided by the STARFORMAT project<sup>3</sup>, a database containing results of high-resolution numerical simulations computed to study the formation, evolution and collapse of molecular clouds<sup>4</sup>. Among the available projects, we chose the two we describe in the following. The ‘‘Solenoidal vs. compressive turbulence forcing’’ project was carried out by Federath et al. (2008) in order to investigate differences between models of these two limiting regimes characterised by different mechanisms of kinetic energy injection. Simulations were performed using the FLASH3 code (Fryxell et al. 2000; Dubey et al. 2008), solving hydrodynamic equations on  $1024^3$  cubes, assuming an isothermal gas (self-gravity is not included). Snapshots of the cube are available, for both scenarios, at different time steps, calibrated on the timescale parameter  $\mathcal{T} = \mathcal{L}/(2c_s\mathcal{M})$ , where  $\mathcal{L}$  is the size of the computational domain,  $c_s$  the sound speed and  $\mathcal{M}$  the rms Mach number. To explore possible structure variations at two different epochs, we considered the second and the second last available time steps, namely for  $t_1 = 3\mathcal{T}$  and  $t_2 = 9\mathcal{T}$ .

The used data sets consist of the column density maps obtained projecting the density cube along one of the three axes, say  $x$  (then, in this convention, in the  $yz$  plane), and rebinned onto a  $256^2$  pixel grid. Moreover, to investigate possible projection effects, also the projection in the  $xy$  plane of the cube at the time  $t_1$  has been used.

<sup>3</sup> starformat.obspm.fr

<sup>4</sup> Among other interesting resources for downloading numerical simulations of the ISM, we advise also Galactica (<http://www.galactica-simulations.eu>), CATS (<http://mhd-turbulence.com>), and the John’s Hopkins Turbulence Databases (<http://turbulence.pha.jhu.edu>), not used for this work.

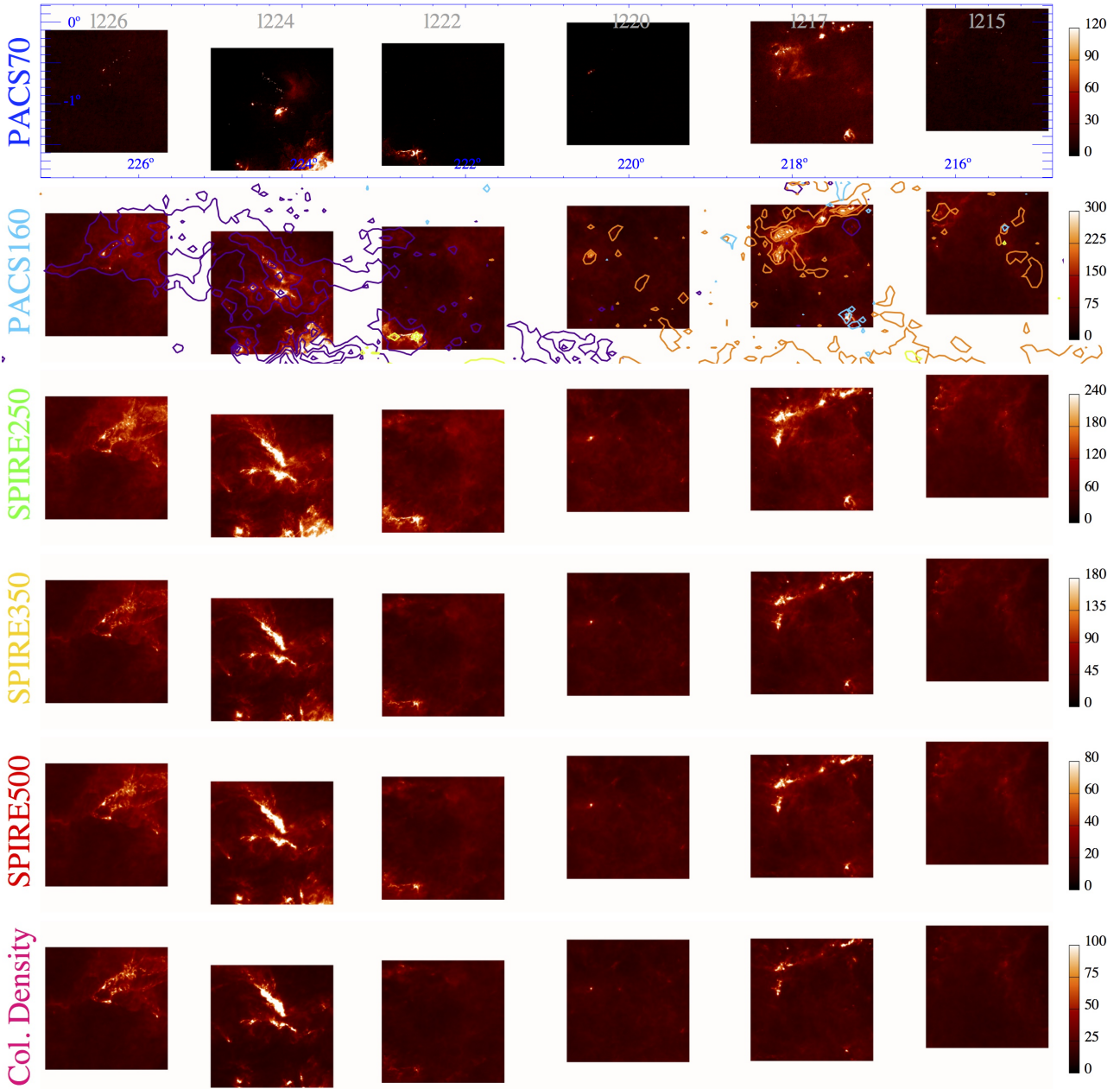


**Figure 1.** Each row shows the six Hi-GAL fields investigated in this paper. The instrument/band combination is specified in each row, adopting the color convention that is used throughout the rest of the paper, namely blue:  $70\ \mu\text{m}$ , cyan:  $160\ \mu\text{m}$ , green:  $250\ \mu\text{m}$ , yellow:  $350\ \mu\text{m}$ , red:  $500\ \mu\text{m}$ , magenta: column density. The color scales are linear; we preferred this choice with respect to the logarithmic scale to show the actual dynamics of the maps processed in this paper. The units are  $\text{MJy sr}^{-1}$  for the PACS and SPIRE maps, and  $10^{20}\ \text{cm}^{-2}$  for the column density ones. The tile names and Galactic coordinate grid are displayed in the row of  $70\ \mu\text{m}$  images (longitude on the horizontal axis and latitude on the vertical axis). Notice that the frame displacement is a real effect due to the choice of square area cut from each original tile. The CO(1-0) contour levels of Elia et al. (2013) are overplotted on the row of  $160\ \mu\text{m}$  images. The contours start from  $5\ \text{K km s}^{-1}$  and are in steps of  $15\ \text{K km s}^{-1}$ . Velocity components I, II, III, and IV (see text) are represented with purple, orange, yellow, and cyan contours, respectively.

In conclusion, exploring two scenarios (solenoidal and compressive), two epochs and an alternative projection direction for the first epoch, six different maps were included in our analysis (Figure 2, top two rows). Images corresponding to the two different scenarios appear quite different, being the compressive forcing maps characterised by a sharper contrast between very bright and extended void regions. Differences in structure have been already highlighted and quantified by Federrath et al. (2008, 2009, 2010) through proba-

bility density function and power spectrum/ $\Delta$ -variance analysis. In Paper I a generally better consistency in terms of power spectrum slope/fractal dimension has been found between the four central Hi-GAL fields analysed in this paper and the solenoidal case rather than the compressive one.

The second project selected in the STARFORMAT data base is “Molecular cloud evolution with decaying turbulence” (Dib et al. 2010; Soler et al. 2013), which aims at describing a self-gravitating

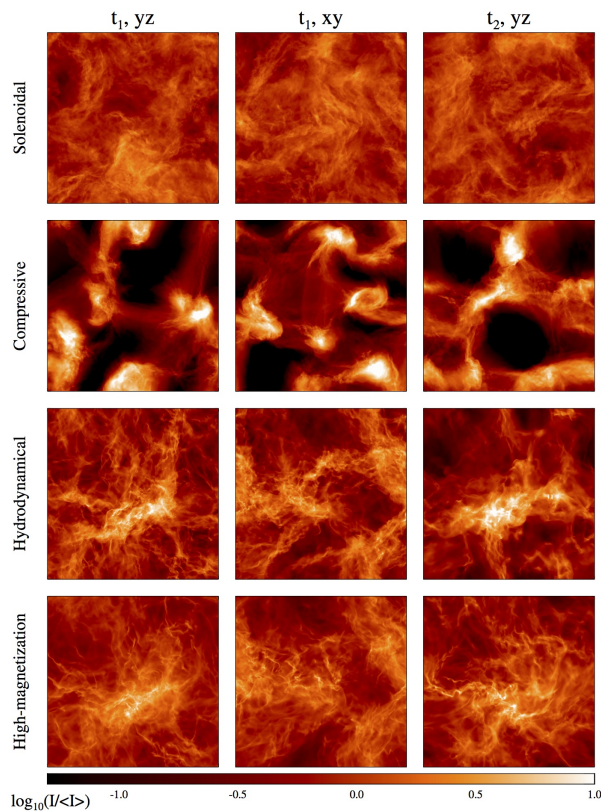


**Figure 2.** Column density maps obtained by projecting 3-dimensional simulated density fields selected in the STARFORMAT archive. The rows, from top to bottom, correspond to four different scenarios, namely “solenoidal forcing”, “compressive forcing”, “quasi-hydrodynamical”, and “high-magnetization”, respectively (see text). The images in the upper two rows are composed by  $256 \times 256$  pixels, while those in the lower two rows are composed by  $2048 \times 2048$  pixels, see Table 1. In each column a different combination of epoch and projection direction is displayed: the assignment of  $yz$  and  $xy$  plane denominations follows the notation used in STARFORMAT, used here only to indicate that the two planes are orthogonal. With  $t_1$  and  $t_2$  we do not indicate, in general, the same time for all the four scenarios, but only two different epochs such that  $t_1 < t_2$ ; they coincide for the first and the second scenario only. Further details of the simulations are reported in the text. Maps are represented here by arbitrarily normalising their values by the map average  $\langle I \rangle$ , and rendered through a logarithmic scale, choosing an image saturation level of  $\log_{10}(10\langle I \rangle)$ , to better appreciate the low-density fluctuations.

cloud with decaying turbulence in presence of a magnetic field. We considered two limiting scenarios with a weak and a strong mean magnetic field ( $B < 4 \mu\text{G}$  and  $B > 20 \mu\text{G}$ , respectively), called “quasi-hydrodynamical” and “high-magnetization” case, respectively. Simulations were performed through the RAMSES-MHD code (Teyssier 2002; Fromang et al. 2006) and produced cubes with an effective resolution of  $2048^3$  elements reproducing a 4 pc-wide region hosting a cloud with a mass of  $\sim 2000 M_{\odot}$ . Two snapshots are available, in correspondence of  $t_1 = 0.49$  Myr and  $t_2 = 1.16$  Myr for the former scenario, and  $t_1 = 0.61$  Myr and  $t_2 = 1.15$  Myr for the latter, respectively. Also in this case, the projection of the density field in the  $yz$  plane has been taken at these two epochs, together with the projection in the  $xy$  plane at the earliest of the two epochs. The selected fields are shown in the last two rows of Figure 2.

### 2.3 Fractional Brownian motion images

The *fractional Brownian motion* images (fBm, Peitgen & Saupe 1988) are often used as a surrogate of ISM maps thanks to their visual similarity with cloud features (Stutzki et al. 1998; Bensch et al. 2001; Miville-Deschênes et al. 2003). Their analytic properties are fully described in Stutzki et al. (1998) and recently resumed in Paper I, to which we refer the reader for more details. Here, we simply remind their basic properties: *i*) their radially averaged power spectrum exhibits a power-law behaviour, and *ii*) the distribution of the phases of their Fourier transform is completely random. These images are fractal, with a precise analytic relation between their (mono-)fractal dimension  $D$  (see Section 3) and the power-spectrum power-law exponent  $\beta$ :

$$D = 4 - \frac{\beta}{2}, \quad (1)$$

which is valid for a signal defined over a two-dimensional space (Stutzki et al. 1998).

In this paper, we use these images as a reference, since they can be obtained with preconditioned statistical properties. In particular we generated a set of  $1000 \times 1000$  pixels fBm images by exploring a two-dimensional parameter space, i.e. varying both the  $\beta$  exponent (then the global fractal dimension) from 2 to 4 in steps of 0.4 (cf. Paper I), and the distribution of the phases, initializing the random number generator with three different “seeds”, called hereafter realization A, B, and C. A given phase distribution determines the global appearance of the image as a “cloud”, while increasing  $\beta$  produces a gradual smoothing of the image, due to the transfer of power from high to low spatial frequencies, as it can be seen in Figure A1 (Appendix A).

## 3 MULTIFRACTAL ANALYSIS

As pointed out in Section 1, the multifractal analysis represents an extension of the fractal theory, aimed at enhancing and enriching the characterization of a non-deterministic (i.e. natural) fractal. It is closely related to the concept of *generalized fractal dimension*.

### 3.1 Generalized fractal dimension

The *fractal dimension*, introduced by Mandelbrot (1967), is one of the fundamental concepts in fractal analysis. It expresses the degree of complexity of a self-similar object, and in particular its ability to fill the hosting space. Importantly, it is not an integer number, exceeding the Euclidean dimension of the set (e.g., the fractal dimension of a fractal line is larger than 1, the one of a fractal surface is larger than 2, etc.). In this respect, the fractal dimension represents a meaningful indicator for quantifying the structure of complex, nested, convoluted structures which depart from the smooth appearance of Euclidean shapes. Nevertheless, the need of going beyond a single descriptor, leads to the formulation of the multifractal geometry, based on the concept of *fractal generalized dimension*.

The definition of a set of dimensions of order  $q \in \mathbb{R}$  is due to Hentschel & Procaccia (1983), who introduced this concept to improve the characterization of chaotic attractors of dynamical systems. A single parameter constitutes an incomplete characterization of such sets, which are not perfectly self-similar by construction like, instead, the deterministic examples (such as the well-known Cantor set or the Koch curve). The *generalized dimensions*, therefore,



represent an attempt to address in a more general way the characterization of the so-called “strange sets”.

Among various formulations of the generalized dimensions, here we briefly report the one based on the box-counting approach (cf. Hentschel & Procaccia 1983): let us start considering a set constituted by points (as, for example, black pixels in an image with a white background), in this context generally named *measure*, and cover it with boxes of size  $\varepsilon$ . Let us define the probability of points contained in the  $i$ -th box as  $P_i = N_i/N$ , where  $N_i$  is the number of points in the  $i$ -th box, out of a total number of points  $N$ . The  $q$ -th generalized dimension  $D_q$  is defined as

$$D_q = \lim_{\varepsilon \rightarrow 0} \frac{1}{q-1} \frac{\log \sum_i P_i^q}{\log \varepsilon}. \quad (2)$$

Defining the partition function of the  $q$ -th order as

$$Z_q(\varepsilon) = \sum_i P_i^q, \quad (3)$$

the definition in Equation 2 becomes

$$D_q = \lim_{\varepsilon \rightarrow 0} \frac{1}{q-1} \frac{\log Z_q(\varepsilon)}{\log \varepsilon}. \quad (4)$$

Notice that the case  $q = 0$  recovers the classic expression of the box counting mono-fractal dimension  $D$  (e.g., Falconer 2003). An interesting case is  $D_1$  (also called *information dimension*), obtained from Equation 2 in the limit  $q \rightarrow 1$ . By construction, all the  $D_q$  dimensions of a deterministic pure fractal will coincide with  $D$ , while a *multifractal* is an object whose generalized dimensions are quite different. The  $D_q$  values monotonically decrease with increasing  $q$  (Hentschel & Procaccia 1983), and the lower and upper limiting dimensions, named  $D_{-\infty}$  and  $D_{+\infty}$ , respectively, are related to the regions of the set in which the measure is “most diluted” and “most concentrated”, respectively.

In general, the partition function of multifractal sets scales as

$$Z_q(\varepsilon) \propto \varepsilon^{\tau_q}, \quad (5)$$

(e.g., Arneodo et al. 1995), with  $\tau_q$  named *correlation exponent* of order  $q$ . The relationship between  $\tau_q$  and  $q$  is expressed by

$$\tau_q = q h(q) - E, \quad (6)$$

where  $E$  indicates the Euclidean dimension of the volume hosting the fractal, named *support of the measure* (e.g., Gu & Zhou 2006). For a monofractal, the  $h(q)$  coefficient is constant (and called *Hurst exponent*) so that the  $\tau_q$  vs  $q$  relation is linear, whereas in the more general case of a multifractal  $h(q)$  (in such case called *generalized Hurst exponent*) varies as a function of  $q$ .

Finally, combining Equations 4 and 5 one finds

$$\tau_q = (q-1)D_q \quad (7)$$

(Halsey et al. 1986). As a particular case of this equation, it is found that  $D_0 = -\tau_0$ .

At this point, some caveats about the interpretation of the introduced quantities and their application to astronomical maps (or to grey-scale images in general) need to be pointed out. Indeed, all the above definitions and considerations are strictly valid for a measure composed by discrete points, when a coverage of the support of the measure is performed. In our case, the measure is a 3-D surface having values different from zero at any point of its support, which is a  $m \times n$  pixels raster. The probability  $P_i$  is the sum of the brightnesses of all pixels falling inside the  $i$ -th box, normalized by the integral over the entire map. With this approach, it can be seen that, for  $q = 0$ , Equation 2 does not return the true

fractal dimension of the investigated image, but rather the Euclidean dimension of the support of the measure, in other words one finds  $D_0 = 2$  for all images.

### 3.2 Multifractal spectrum

A tool typically used for the multifractal analysis is the so-called *singularity spectrum*, or *multifractal spectrum* (MFS), first introduced by Halsey et al. (1986).

Let us consider a measure (here our Hi-GAL maps) embedded in a support and cover it with boxes of size  $\varepsilon$  as already discussed in Section 3.1. If the measure is a multifractal, the probability  $P_i$  scales with  $\varepsilon$  as a power law with exponent  $\alpha_i$  (also known as *singularity strength*), as a function of the position:  $P_i(\varepsilon) \propto \varepsilon^{\alpha_i}$ . Given the fractal dimension  $f(\alpha)$  of the subset of boxes having singularity strength in the range  $(\alpha, \alpha + d\alpha)$ , the MFS is just the curve of  $f(\alpha)$  vs  $\alpha$ . It represents the contributions to the geometry provided by interwoven sets with different singularity strengths.

The relation between the MFS and the generalized dimensions is expressed by the *Legendre’s transform*:

$$\alpha(q) = \frac{d\tau_q}{dq} \quad (8)$$

$$f(\alpha(q)) = q\alpha(q) - \tau_q \quad (9)$$

(Halsey et al. 1986). In this sense, the MFS can be calculated immediately after deriving the  $(q, D_q)$  pairs.

From these relations the following properties of the  $f(\alpha)$  curve are derived:

$$\frac{df}{d\alpha} = q \quad (10)$$

$$\frac{d^2f}{d\alpha^2} < 0. \quad (11)$$

Therefore, the MFS is concave for any measure, with a single maximum at  $q = 0$  (then  $f(\alpha(0)) = D_0$  for a measure constituted by points<sup>5</sup>), and with infinite slope at  $q = \pm\infty$ .

The MFS gives information about the relative importance of various fractal exponents present in the map, and in particular its width indicates the range in which such exponents lie. The part corresponding to values  $q > 0$  characterises the scaling properties of overdense regions because it magnifies the effect of large numbers, while for  $q < 0$  the behaviour of low-density subsets is characterised. This generally results in an asymmetrical shape of the MFS with respect to its peak position ( $q = 0$ ).

### 3.3 Practical derivation of multifractal parameters

For the purpose of this paper we derive the values of  $\tau_q$  and  $D_q$  for each map through the partition function, as described in Section 3.1. The analysed sets are constituted by a discrete number of pixels, thus we partition the data sets in boxes with integer size  $\varepsilon$ . In this respect, it is preferable to deal with image sizes that have a large number of integer divisors (see Section 2.1) enough to ensure a sufficiently

<sup>5</sup> As already pointed out in Section 3.1, here we analyse greyscale images. In this case,  $f(\alpha(0))$  coincides with the Euclidean dimension of the support of the measure, namely 2, as it can be seen, in the following, from Equation 14 combined with Equation 12.

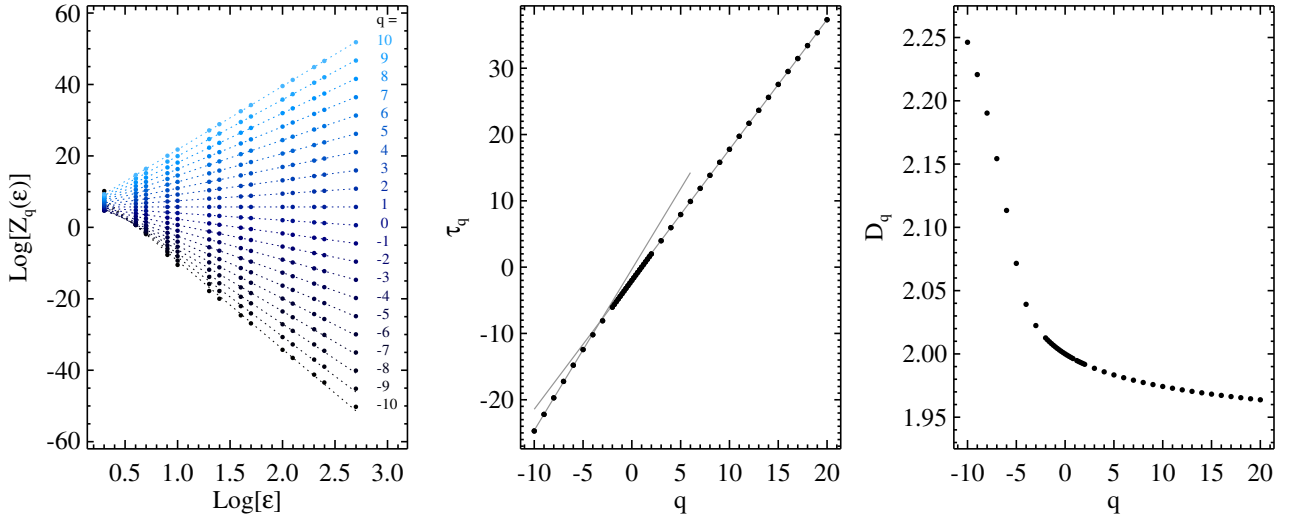


**Figure 3.** Example of derivation of the generalised fractal dimensions for a test  $1000 \times 1000$ -pixel fBm image (see Section 2.3), in this case the one of type “C” and  $\beta = 2.4$  shown in Figure A1. *Left:* logarithm of the partition functions  $Z_q(\epsilon)$  vs the logarithm of the integer scales  $\epsilon$  between 1 and 500 pixels for each integer value of the parameter  $q$  between  $-10$  and  $10$  (in this range, different shades of blue, from the darkest to the lightest, respectively, are used for each different  $q$ ). The linear fit is shown as a dashed line of the same colour of the corresponding  $Z_q$  function (cf. Equation 5). The functions for orders  $q > 10$  and non-integer orders in the range  $-2 < q < 2$ , although computed, are not shown here for the sake of clarity. *Middle:* scaling exponents  $\tau_q$  of the partition function, obtained through the linear fit shown in the left panel as a function of  $q$ . To highlight the different slopes at negative and positive orders, the linear fit of the  $\tau_q$  vs  $q$  in the two the regions  $q < -3$  and  $q > 3$ , is shown by means of two grey lines. *Right:* generalised fractal dimension set, derived through Equation 7, as a function of  $q$ , except for the case  $q = 1$ , not contemplated by Equation 7.

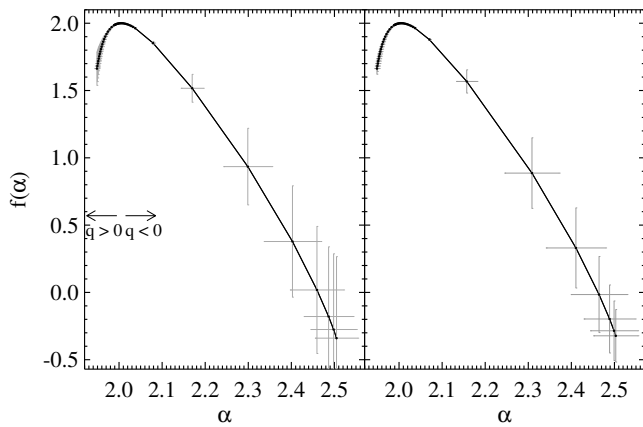


**Figure 4.** *Left:* MFS of the same fBm reference image used to build Figure 3, obtained through Equations 8 and 9, exploring the range of orders  $-10 \leq q \leq 20$ , in steps of  $\Delta q = 1$  (but  $\Delta q = 0.2$  in  $-2 \leq q \leq 2$ ). The error bars are displayed as grey crosses for each point, to give an idea of the typical uncertainties affecting the MFS estimation. *Right:* The same as in the left panel, but computed through Equations 13 and 14.

large range of investigated spatial scales, i.e. points to sample the behavior of the right-hand side of Equation 4.

In Figure 3 we show a derivation of these quantities for a fBm test image shown in Figure A1, third-row and third-column panel, corresponding to realization “C” and power spectrum slope 2.4. For this example, as well as for all maps analysed in this paper, the probed range of orders  $q$  is  $-10 \leq q \leq 20$ , in steps of  $\Delta q = 1$ , except for the interval  $-2 \leq q \leq 2$ , which is explored in steps of  $\Delta q = 0.2$  to better sample a critical region for multifractal descriptors (slope change for  $\tau_q$ , inflection point of  $D_q$ , and peak of the MFS around  $q = 0$ , see below).

The  $Z_q(\epsilon)$  function (left panel) shows the expected power-law

behaviour, from which the  $\tau_q$  scaling fits can be derived through a linear regression procedure (Equation 5). The quality of such fit determines in turn the extent of the error bar on  $\tau_q$ . The  $\tau_q$  vs  $q$  curve (middle panel) does not present a single linear behaviour, but a typically multifractal behaviour with two different slopes for the two  $q < 0$  and  $q > 0$  regimes, and a non-linear behaviour in the transition zone (cf., e.g., Movahed et al. 2011; Xie et al. 2015). Similarly, the obtained  $D_q$  vs  $q$  curve (right panel) is far from being constant (cf., e.g., Halsey et al. 1986; Meneveau & Sreenivasan 1987), confirming that the analysed image presents a multifractal rather than a simple mono-fractal character.

Once  $\tau_q$  and  $D_q$  are obtained, the MFS can be derived through Equations 8 and 9. Another linear fit is requested in this case, introducing a larger uncertainty on both  $\alpha$  and  $f(\alpha)$ . An alternative method for calculating directly the MFS was developed by Chhabra & Jensen (1989) and applied by Chappell & Scalco (2001) for estimating the MFS of *IRAS* maps. Defining the coarse-grained moments  $\mu_i(q, \epsilon)$  of the original image as

$$\mu_i(q, \epsilon) = \frac{P_i^q(\epsilon)}{\sum_i P_i^q(\epsilon)}, \quad (12)$$

$\alpha$  and  $f(\alpha)$  are implicitly defined with respect to the  $q$  parameter through

$$\alpha(q) = \lim_{\epsilon \rightarrow 0} \frac{\sum_i \mu_i(q, \epsilon) \log P_i(\epsilon)}{\log \epsilon} \quad (13)$$

$$f(q) = \lim_{\epsilon \rightarrow 0} \frac{\sum_i \mu_i(q, \epsilon) \log \mu_i(q, \epsilon)}{\log \epsilon}. \quad (14)$$

In practice, in the case of an ideal multifractal, the quantities whose limits are calculated in the right sides of the equations above show a linear behavior, since the limits can be extrapolated from a linear fit. Consequently, the uncertainties associated to  $\alpha(q)$  and  $f(\alpha(q))$  mainly depend on the quality of such fit. Again, we reaffirm, also

for this approach, the need of analysing images with sizes divisible by a large number of integer factors.

In Figure 4, we compare the MFS obtained for the same fBm image using the two methods. The spectra look practically identical, with differences smaller than 1% in all cases, while the error bars, which are generally much larger for  $q < 0$ , are comparable for  $\alpha$  but larger for the first method for  $f$ . For this reason, in the following we will show MFSs obtained through the Chhabra & Jensen (1989) method (Equations 13 and 14), keeping the first one as a reference for checking the correctness of the results.

## 4 RESULTS OF MULTIFRACTAL ANALYSIS

The multifractal behaviour of the analysed maps can be examined by means of both the generalised dimension formalism ( $D_q$  vs  $q$ ) or the MFS one ( $f(\alpha)$  vs  $\alpha$ ). We start from the latter, which allows us to better highlight some peculiarities in our map sample with respect to the scaling implied by Equation 3.

### 4.1 Qualitative analysis of MFS

In Figure 5 the MFS of each Hi-GAL tile at each band are shown, while in Table 2 a number of salient parameters of the MFS, some of which introduced in the following Section 4.2, are listed<sup>6</sup>. It is possible to make some initial and general considerations about the overall appearance of the spectra:

- In general, the MFSs present a typical single-humped shape with a maximum at  $f_0 = 2$  (i.e. the Euclidean dimension of the support, as explained previously), but a strong negative skewness.

- In several cases, at high  $q$  (i.e. at the left end of the MFS) a cusp-like turnback of  $\alpha(q)$  appears in the spectrum (the most evident case being found for the 70  $\mu\text{m}$  map of  $\ell 224$ , but other cases are well recognisable in the plots of Figure 5). Such a feature (cf. Lou et al. 2015) can be considered *i*) as a computational artefact, due to the presence of spatial heterogeneity of brightness in the image which leads to disproportionate contribution of boxes containing rare extremely intense pixels during averaging over the whole area, and *ii*) as a real effect related to intrinsic statistical properties of the analysed image departing from those of a multifractally distributed measure. Wolf (1989), indeed, demonstrated that this feature appears in correspondence of a breakdown in the scaling law expressed by Equation 5 at orders higher than a critical value  $q_c^+$  (see also, e.g., Abry et al. 2004). Most likely, the appearance of such a cusp is produced by a combination of these two effects in images presenting a wide dynamic range between the diffuse emission and few very bright compact sources. In Table 2 a possible presence of a cusp in the MFS is reported by listing the possible value of  $q_c^+$ . The maps affected by this problem will suffer of some limitations throughout the analysis carried out in this paper, since the part of the spectrum corresponding to  $q > q_c^+$  (missing data in Table 2) will not be taken into account.

- In most cases, the right portion of the MFS for the 70  $\mu\text{m}$  maps turns out to be collapsed to a very short branch close to the peak, while the left portion (in correspondence of positive  $q$  values) appears extremely elongated. In general, a MFS shows a long left tail when the signal has a multifractal structure which is

insensitive to the local fluctuations with small amplitudes, and a shrunk right tail in presence of a small scale noise-like background (e.g., Drożdż & Oświęcimka 2015). This is the typical case of Hi-GAL 70  $\mu\text{m}$  maps in this portion of the Galaxy generally showing rare and isolated bright spots, corresponding to episodes of star formation, and a very faint background emission often surmounted by the instrumental noise. This fact, together with the frequent occurrence, for the 70  $\mu\text{m}$  maps, of the aforementioned cusps in the MFS, makes the maps at this wavelength a peculiar case in our multi-fractal analysis, showing in general a departure from a fractal behaviour.

- For each tile, the MFSs of the SPIRE images show a relatively similar behaviour, but not identical. The positions of the extreme points can differ, even significantly, from band to band depending on the tile, the strongest differences being found in the tiles containing the brightest features, i.e.  $\ell 217$ ,  $\ell 224$ , and  $\ell 226$ . Such overall similarities and fine-scale differences will be highlighted in the following more quantitative analysis.

- The 160  $\mu\text{m}$  maps show a behaviour of the MFS width which is intermediate between the 70  $\mu\text{m}$  and the SPIRE ones, being the  $q < 0$  tail less pronounced than for the SPIRE maps, but not collapsed as generally found for the 70  $\mu\text{m}$  ones.

- Finally, the column density maps, which could be expected to have a behaviour similar to the SPIRE ones, actually differ significantly from them in some cases, especially for the tiles  $\ell 217$  and  $\ell 224$ .

The MFS was derived also for all the simulated column density fields described in Section 2.2 and shown in Figure 2. All the computed MFSs are plotted in Figure 6, each panel corresponding to a different model. In the following, we summarize some results of the comparison among the different models and their projections and epochs, and with the Hi-GAL observations

First, the MFSs of the simulations look quite different, in general, from those of the Hi-GAL maps. Particularly on the right side of the curve, for the simulations the largest value of  $\alpha$ , corresponding to the most negative explored  $q$ , is larger than the one of the observations (a more quantitative description of this aspect will be given in Section 4.2). Notice also that for some spectra cusps like those described above, but located at the opposite extreme, appear. In some cases, the cusp can not be noticed in the figure because the turnaround point is found close to  $q = -10$  and the following points are very close to those of the “regular” part of the MFS. Anyway, in Table 3 we account for the possible occurrence of such an effect for  $q$  smaller than a critical  $q_c^-$ , together with possible occurrences of cusps in the  $q > 0$  portion of the spectrum as well, and with other relevant parameters of the MFSs, similarly to Table 2.

Second, remarkable differences are found among the models: the “compressive forcing” case shows much wider spectra with extended right tails, produced by the presence of large void regions already well recognisable in Figure 2, second row. Their shape and extent are due, in turn, to those original cavities in the 3-dimensional synthetic cloud, and to the possible contribution by the foreground medium, depending on the projection direction, which is more relevant in presence of a highly inhomogeneous matter distribution. In this  $q < 0$  part, in fact, the MFSs of the “compressive forcing” maps appear to be more sensitive to projection effects than to evolutionary ones, being the  $t_2$  curve contained between the two  $yz$  and  $xy$  projections at the time  $t_1$ . This trend is found also in the “solenoidal” case, but within the framework of narrower MFSs, qualitatively more similar to observations, at least to the case less influenced by the presence of strong singularities (bright compact sources),

<sup>6</sup> Notice that hereafter, for the MFS coordinates corresponding to a given order  $Q$  we use the simplified notation  $\alpha_Q$  and  $f_Q$  in place of  $\alpha(q = Q)$  and  $f(q = Q)$ , respectively.



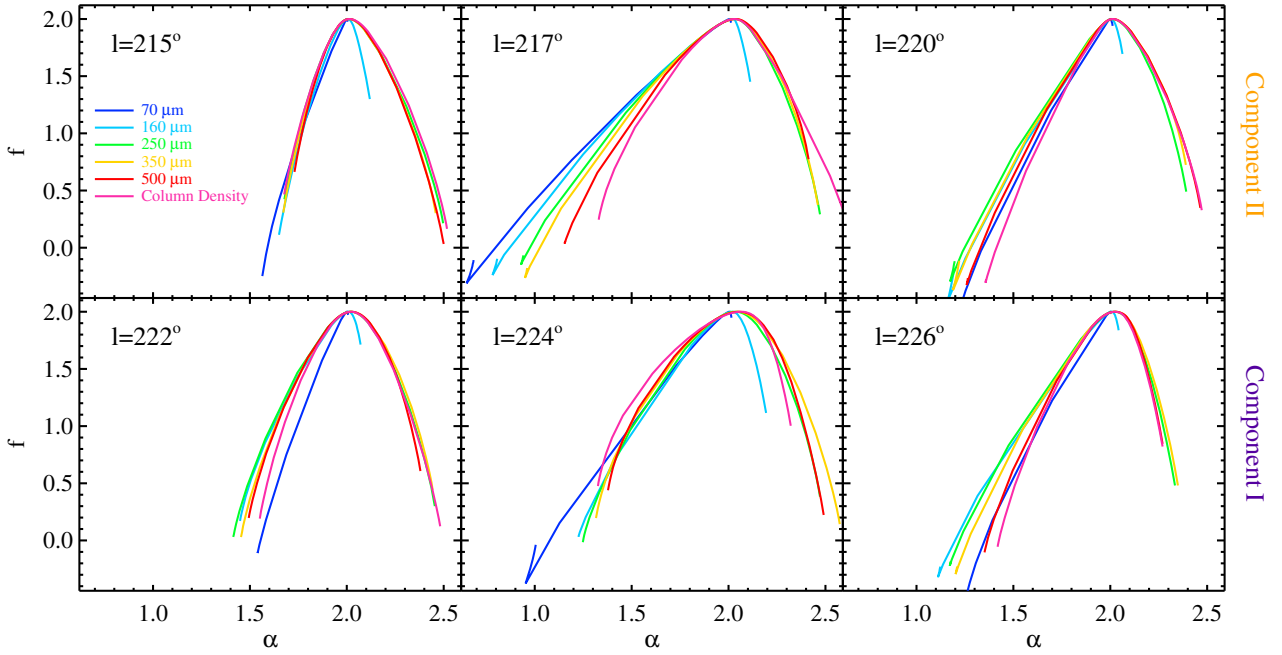


**Figure 5.** MFS of the Hi-GAL maps analysed in this work, ordered by tile (in turn, tiles associate to kinematic components I and II are arranged in the lower and in the upper row, respectively). The colour-band correspondence is the same introduced in Figure 1 and used throughout the entire paper.

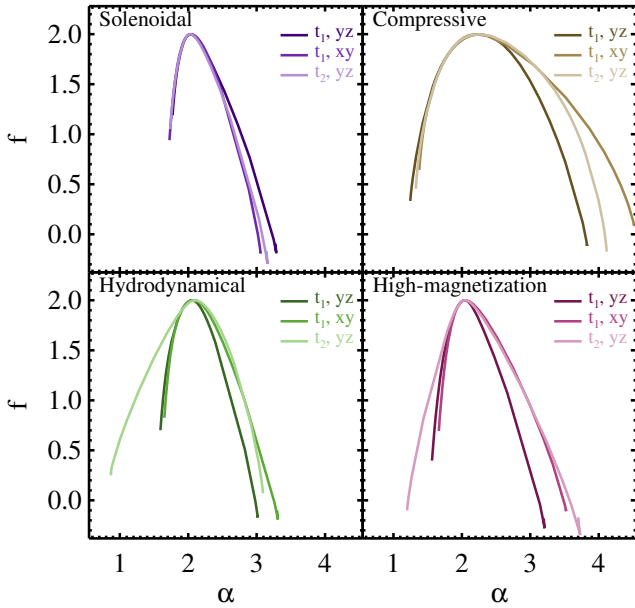


**Figure 6.** MFS of the column density maps obtained from simulations, shown in Figure 2. In each panel the model, the projection plane and the epoch of the simulation are specified for each displayed MFS. The range of  $\alpha$  on the horizontal axis is chosen to optimise the plot of the represented MFS, and for this reason a visual comparison with the plots in Figure 5 (set according to the same criterion) can not be performed directly.

namely  $l_{215}$ . On the contrary, the appearance of bright spots in the maps of the last two scenarios, “quasi-hydrodynamical” and “high-magnetization” (bottom panels), being the gravitational collapse one of the possible ingredients of these models, produces the broadening of the left tail of the MFS at increasing evolutionary time ( $t_2$ ); the right tail gets wider as well, but in this case the evolutionary

effect can be confused with the projection effects already seen for the other scenarios. In short, the MFS of the last two models at time  $t_1$  look relatively similar to those of the “solenoidal forcing” case, but broaden for the later epoch  $t_2$ , characterised by an enhancement of star formation activity inside the cloud. Furthermore, since the star formation efficiency is higher in the “quasi-hydrodynamical” case than in the “high-magnetization” one, the left tail of the MFS at  $t_2$  turns out to be much wider in the former than in the latter. In Appendix B a more systematic analysis of the evolution of the MFS left tail width with time in presence of gravity in the simulations is provided.

To complete this qualitative description of the computed MFS, let us look at the spectra of the fBm reference images, with particular emphasis to changes in the MFS as a consequence of variations of their fractal parameters. In Figure 7 the MFS, calculated for all the 18 images generated for this work (see Section 2.3 and Appendix A), are shown. The increase of the power-law exponent  $\beta$  clearly produces a systematic increase of the width of the  $q < 0$  part, but also a drift of the extreme point of the  $q > 0$  part towards larger values of  $f$  and  $\alpha$ . This right-sided asymmetry indicates, in general, that small scale fluctuations exhibit a more pronounced multifractal behaviour than large scale ones. Again, let us notice that this overall trend does not exclude possible peculiar differences from image to image. Surprisingly, even for images generated with the same  $\beta$  (then with the same the fractal dimension, according to Equation 1) we can find differences depending on the choice of the random phases. It is possible to ascertain this fact comparing the shape of the MFS of images having the same  $\beta$  in the three panels of Figure 7, but corresponding to different random phase distributions. Finally, it is to notice that also the MFSs of the fBm images can suffer of the presence of cusp-like features, namely at the smallest negative  $q$  orders. Similarly to previously considered classes of images, in Table 4 the most relevant features of the MFS of fBm sets are listed.

**Table 2.** Main properties of the MFS of the analysed Hi-GAL frames.

Field	Band	$\alpha_{20}$	$f_{20}$	$\alpha_{10}$	$f_4$	$\alpha_0$	$\alpha_{-10}$	$q_c^+$	$A_\Phi$
$\ell 215$	70	1.53	-0.64	1.56	1.72	2.001	2.01	...	...
	160	1.63	-0.06	1.65	1.77	2.006	2.12	...	0.07
	250	1.65	0.05	1.68	1.70	2.012	2.50	...	0.12
	350	1.64	-0.06	1.67	1.73	2.012	2.46	...	0.12
	500	1.70	0.22	1.73	1.76	2.014	2.50	...	0.12
	Column Density	1.66	0.23	1.68	1.71	2.014	2.52	...	0.13
$\ell 217$	70	...	...	...	-0.31	2.007	2.01	4	...
	160	...	...	...	-0.24	2.023	2.11	4	0.14
	250	...	...	...	-0.12	2.031	2.47	5	0.18
	350	...	...	...	-0.17	2.035	2.46	5	0.19
	500	...	...	...	0.22	2.035	2.41	6	0.19
	Column Density	1.32	0.16	1.33	0.69	2.030	2.69	...	0.17
$\ell 220$	70	...	...	1.21	-0.03	2.002	2.01	10	...
	160	...	...	...	-0.09	2.006	2.06	6	...
	250	...	...	...	-0.03	2.012	2.39	5	0.14
	350	...	...	...	0.03	2.013	2.39	6	0.14
	500	...	...	...	0.31	2.013	2.46	7	0.14
	Column Density	...	...	...	0.67	2.012	2.47	8	0.13
$\ell 222$	70	...	...	...	1.57	2.002	2.01	9	...
	160	1.44	0.07	1.45	0.85	2.010	2.07	...	...
	250	1.41	0.00	1.41	0.89	2.020	2.45	...	0.15
	350	1.45	-0.06	1.45	1.08	2.021	2.44	...	0.15
	500	1.49	0.13	1.49	1.17	2.024	2.38	...	0.15
	Column Density	1.54	0.07	1.55	1.40	2.021	2.48	...	0.14
$\ell 224$	70	...	...	...	-0.38	2.005	2.02	4	...
	160	1.23	0.04	1.23	0.20	2.022	2.19	...	0.13
	250	1.24	-0.07	1.25	0.42	2.035	2.47	...	0.18
	350	1.31	0.07	1.32	0.71	2.044	2.57	...	0.20
	500	1.36	0.22	1.38	0.88	2.053	2.49	...	0.21
	Column Density	1.31	0.31	1.33	0.90	2.064	2.32	...	0.20
$\ell 226$	70	...	...	1.25	0.18	2.001	2.00	12	...
	160	...	...	...	-0.21	2.007	2.04	5	...
	250	...	...	...	0.08	2.021	2.33	6	0.14
	350	...	...	...	0.06	2.025	2.35	6	0.14
	500	...	...	1.35	0.61	2.026	2.27	10	0.14
	Column Density	...	...	1.42	1.00	2.024	2.27	11	0.13

**Table 3.** Main properties of the MFS of the analysed simulations.

#	Model	Plane	Epoch	$\alpha_{20}$	$f_{20}$	$\alpha_{10}$	$f_4$	$\alpha_0$	$\alpha_{-10}$	$q_c^+$	$q_c^-$	$A_\Phi$
1	Solenoidal forcing	yz	$t_1$	1.74	0.70	1.77	1.69	2.032	...	...	-5	0.21
2	Solenoidal forcing	xy	$t_1$	1.68	0.34	1.73	1.67	2.042	...	...	-7	0.21
3	Solenoidal forcing	yz	$t_2$	1.71	0.63	1.74	1.64	2.033	...	...	-6	0.20
4	Compressive forcing	yz	$t_1$	1.24	0.26	1.25	0.78	2.252	...	...	-6	0.49
5	Compressive forcing	xy	$t_1$	1.35	0.31	1.38	1.10	2.213	4.52	...	...	0.56
6	Compressive forcing	yz	$t_2$	1.31	0.17	1.33	0.98	2.254	4.12	...	...	0.57
7	Quasi-hydrodynamical	yz	$t_1$	1.56	0.26	1.59	1.43	2.053	...	...	-7	0.23
8	Quasi-hydrodynamical	xy	$t_1$	1.61	0.35	1.65	1.56	2.075	...	...	-5	0.27
9	Quasi-hydrodynamical	yz	$t_2$	0.86	0.17	0.87	0.33	2.100	3.09	...	...	0.32
10	High-magnetization	yz	$t_1$	1.53	0.01	1.56	1.42	2.043	...	...	-5	0.22
11	High-magnetization	xy	$t_1$	1.62	0.10	1.66	1.60	2.052	...	...	-5	0.26
12	High-magnetization	yz	$t_2$	...	...	1.20	0.23	2.048	...	14	-3	0.27

## 4.2 Quantifying the information contained in the MFS

In order to better quantify the information contained in the analysed MFSs, one needs to establish some meaningful descriptors of the geometry of the spectrum. The literature about multifractal analysis abounds with examples of such indicators. In the following discussion, we use a set of indicators which are independent of each other,

and/or are able to highlight common trends and differences among the analysed sets.

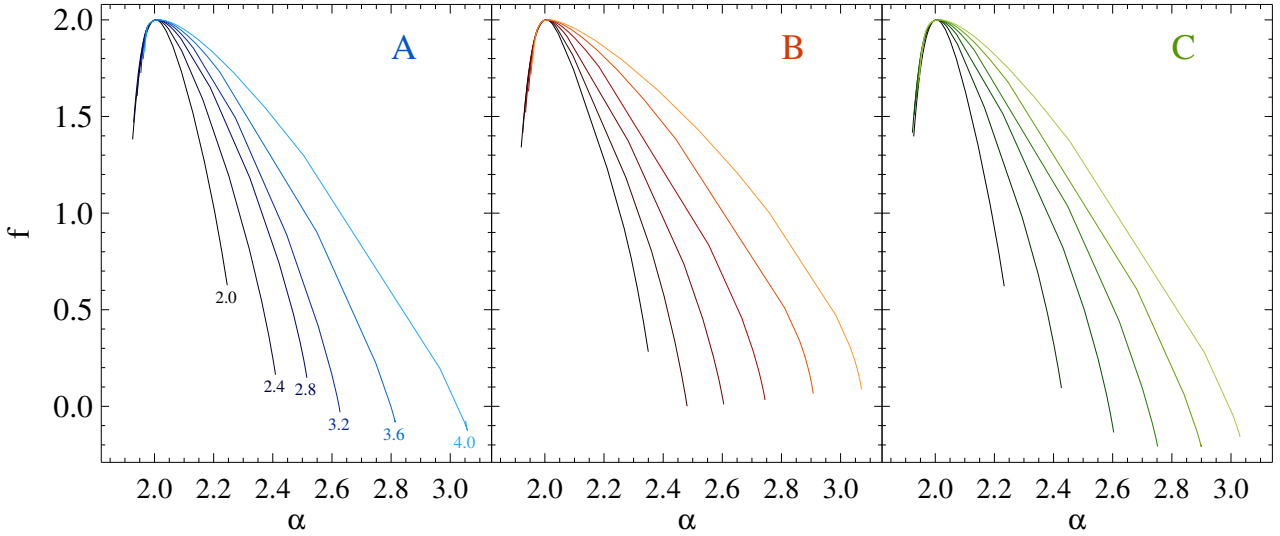


**Figure 7.** MFS of the fBm reference images reported in Figure A1, grouped by image phase distribution (cases “A”, “B”, and “C” in left, middle and right panel, respectively). A different color shade, from the darkest to the lightest, is used for indicating images with the power spectrum exponent  $\beta$  ranging from 2 to 4 in steps of 0.4.

**Table 4.** Main properties of the MFS of the analysed fBm images.

Group	$\beta$	$\alpha_{20}$	$f_{20}$	$\alpha_{10}$	$f_4$	$\alpha_0$	$\alpha_{-10}$	$q_c^-$	$A_\Phi$
A	2.0	1.93	1.38	1.95	1.95	2.004	2.25	...	0.06
	2.4	1.93	1.47	1.95	1.95	2.006	2.41	...	0.08
	2.8	1.94	1.61	1.96	1.95	2.009	2.52	...	...
	3.2	1.95	1.73	1.97	1.96	2.011	2.63	...	...
	3.6	1.96	1.80	1.97	1.96	2.014	...	-8	...
	4.0	1.97	1.84	1.97	1.97	2.016	...	-5	...
B	2.0	1.92	1.34	1.95	1.95	2.004	2.35	...	0.07
	2.4	1.93	1.42	1.95	1.95	2.005	2.48	...	0.08
	2.8	1.93	1.52	1.95	1.95	2.007	2.60	...	...
	3.2	1.94	1.63	1.96	1.95	2.009	2.74	...	...
	3.6	1.95	1.72	1.96	1.95	2.011	2.91	...	...
	4.0	1.96	1.78	1.97	1.96	2.013	3.07	...	...
C	2.0	1.93	1.40	1.95	1.95	2.004	2.23	...	0.06
	2.4	1.92	1.42	1.95	1.94	2.006	2.43	...	0.08
	2.8	1.93	1.51	1.95	1.94	2.008	2.60	...	...
	3.2	1.94	1.59	1.95	1.94	2.010	...	-9	...
	3.6	1.94	1.65	1.96	1.95	2.013	...	-7	...
	4.0	1.95	1.70	1.96	1.95	2.016	...	-8	...

#### 4.2.1 Dimensional diversity vs maximum singularity strength

Here we start from the diagnostics adopted by Chappell & Scalo (2001), which permits a direct comparison with the unique previous case of MFS analysis of interstellar clouds (but with the limitation of considering only the left part of the MFS, neglecting the negative  $q$  orders). These authors used  $\alpha_{20}$  as a measurement of the strength of the brightest singularities found in a given map, and the  $f_4 - f_{20}$  offset (hereafter  $\Delta f_{4,20}$ ) as a “dimensional diversity” to characterise their fields: an image containing isolated, strong and point-like concentrations will have low values of  $f$  for high  $q$  orders, while this parameter is expected to increase in presence of a large variety of geometries. These authors recognised an increasing trend in the  $\Delta f_{4,20}$  vs  $\alpha_{20}$  scatter plot for their sample of IRAS-based column density maps of 13 nearby star-forming regions, so that

structures with strong dominant concentrations (low  $\alpha_{20}$ ) typically have smaller dimensional diversities (low  $\Delta f_{4,20}$ ).

We extend this analysis to our data sets (Hi-GAL observations, simulations and fBm images) for which it was possible to compute the MFS up to  $q = 20$  (see Tables 2 and 3, respectively). We find in Figure 8 that Hi-GAL and simulation maps follow the general trend delineated by the maps of Chappell & Scalo (2001). In particular, among the Hi-GAL tiles, those present at various different wavelengths are  $\ell 215$ , whose different bands occupy the upper part of such trend regardless of wavelength (except, again, for the completely peculiar behaviour of the  $70 \mu\text{m}$  map),  $\ell 222$  in the middle, and  $\ell 224$  at the bottom left end, where the column density map of  $\ell 217$  is found as well. In practice, the maps containing the strongest singularities, i.e. the most active star forming sites,  $\ell 217$  and  $\ell 224$ , show not only, as expected, lower  $\alpha$  values, but also a lower degree of dimensional diversity. Compared with the observational set

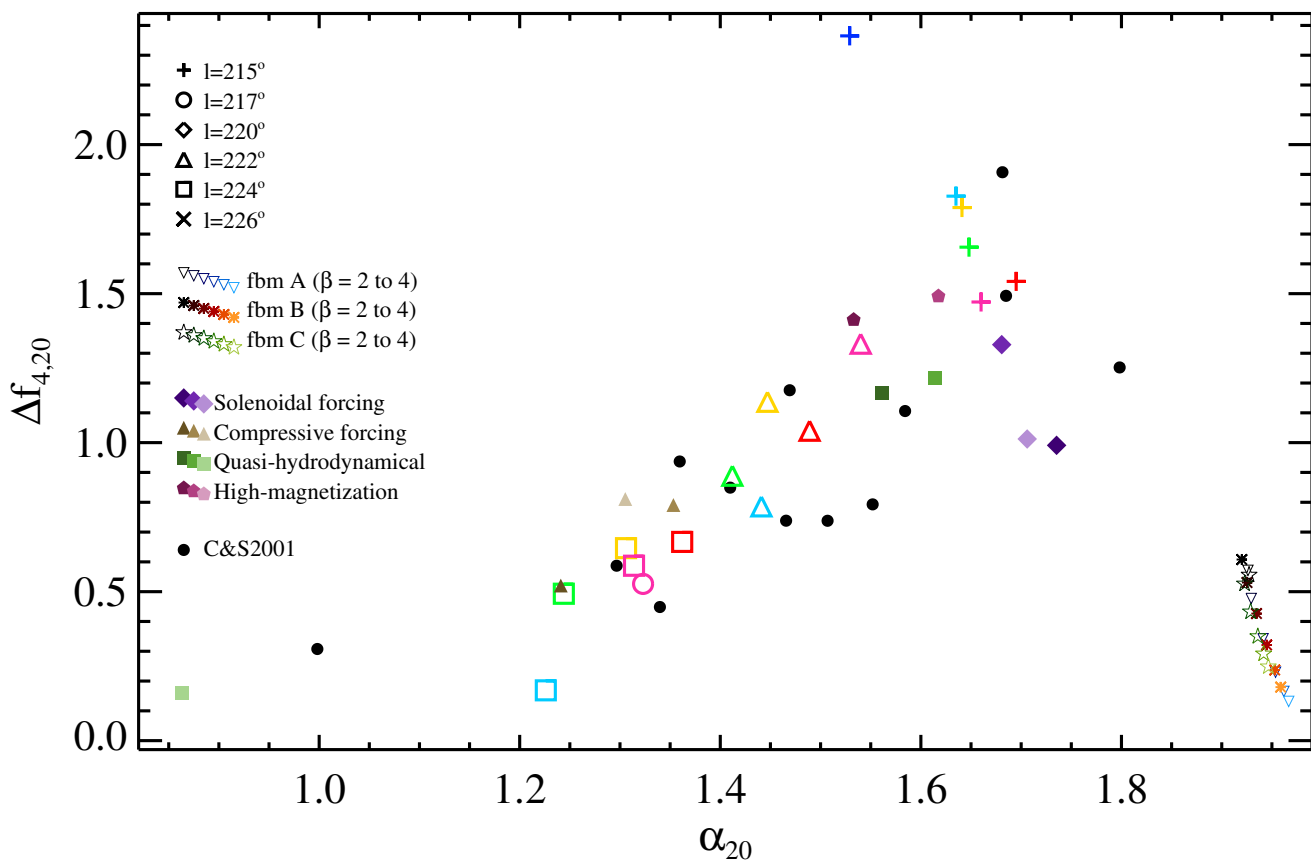


**Figure 8.** Plot of “dimensional diversity”, expressed by  $\Delta f_{4,20} \equiv f(q=4) - f(q=20)$ , versus the smallest computed value of the singularity strength  $\alpha_{20} \equiv \alpha(q=20)$ . Such quantities are available only for Hi-GAL maps with  $q_c^+ \geq 20$ . The correspondence of symbols and colors with tiles and bands, respectively, is explained in the legend; the symbol for the tile  $\ell 226$ , although not present in the plot, is introduced since the convention established here is used also in other following figures. Points representing the 12 cloud simulations and the 18 fBm images analysed in this work are plotted as well (symbols are explained in the legend). Furthermore, the positions of the 18 fBm reference images (located close to the bottom right corner of the diagram) are represented with smaller symbols, using color scales (different for the “A”, “B”, and “C” cases) to identify the different explored values of  $\beta$ . Finally, for comparison, points taken from Figure 8 of Chappell & Scalzo (2001) and representing multifractal features of their IRAS-based column density maps of 13 nearby ( $d \leq 160$  pc) star forming regions are reported as filled black circles (“C&S2001”, in the legend).

of Chappell & Scalzo (2001), their morphology appears, from the statistical point of view, similar to that of their L 134 and Cham 1 cases. On the contrary, tiles more quiescent from the point of view of the star formation, such as  $\ell 222$  and  $\ell 215$ , populate an upper region of the diagram. The latter, in particular, is found to be close to the positions of the fields Oph N, W, and U of Chappell & Scalzo (2001), defined by these authors as the most “space filling” in their sample. The points representing models are spread along the same general trend, as well. Interestingly, the “solenoidal” case is found in the top-right part of the diagram, while the “compressive” one, characterised by stronger singularities, is found at smaller  $\alpha_{20}$ . For both of them no particular dependence on projection or evolutionary effects is seen. Also, both the “quasi-hydrodynamical” and the “high-magnetization” cases, at the time  $t_1$  populate the top-right part of the diagram, but the evolutionary effect is strong in these cases, so that the corresponding MFS broadening seen in Figure 6 is mirrored in this diagram by a significant decrease of  $\alpha_{20}$  at  $t_2$ , which can be seen for the former model, while for the latter it can be guessed but not displayed because  $q_c^+ = 14$ .

Finally, a surprising behaviour is seen for the fBm images in this diagram. They occupy a completely different region of the plot, corresponding to  $\alpha_{20} > 1.9$  and  $0.1 < \Delta f_{4,20} < 0.6$ . This means that, compared with both observations and models, these images

show at the same time a narrower right tail of the MFS, and a low content of fractal diversity. Inside the region occupied by these sets, a trend from top-left to bottom-right is observed at increasing  $\beta$  (so at decreasing fractal dimension). Anyway, all the fBm images appear segregated from the main trend of observational maps, and this should impose serious restrictions to the use of the fBm images as surrogate of the ISM maps, not yet highlighted in literature.

In fact, the assumed affinity between the fBm images and observations of ISM is based on a certain visual similarity and the fact that the power spectrum of the latter ones exhibits a power-law behaviour and some randomness in the phase distribution (Stutzki et al. 1998). However, such a power-law is found only over a limited range of scales (e.g., Stutzki et al. 1998; Schneider et al. 2011), which is typical for natural fractals, and/or different slopes can be found in different ranges of spatial scale (Paper I). In particular, in Paper I it has been shown how strong departures from a single power-law behaviour appear if an original fBm image is manipulated to obtain a more realistic image, i.e. removing its periodicity, and/or easing off the emission along the borders of the image, and/or enhancing the emission in brightest regions to simulate the presence of strong overdensities (their Figure 3). Correspondingly, a change in the Fourier phases is expected as well. For example, Burkhart & Lazarian (2016), analysing numerical simulations of isothermal

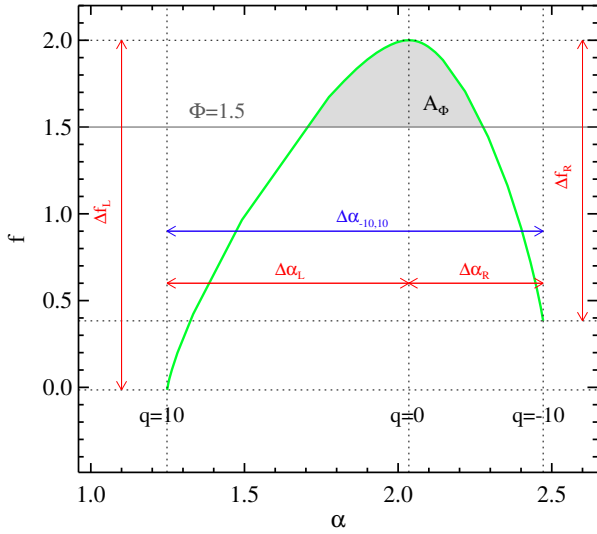


**Figure 9.** Scheme of descriptors used to quantitatively characterize the MFS in this work, and introduced in the text. The example MFS (green curve) is the one of the  $\ell 224$  map at  $250 \mu\text{m}$ , also contained in Figure 5.

compressible turbulence and focusing on information about phases, found that degree of coherence in phase distributions (being the coherence equal to 0 in the case of a random distribution) depends on some simulation parameters, such as the sonic Mach number. Our present empirical analysis, therefore, highlights the need of a further comparative study of the phases among observational, numerical, and fBm maps.

#### 4.2.2 Peak position

The analysis contained in the following represents an expansion of the Chappell & Scalò (2001) approach, thanks to the introduction of further diagnostics to describe the shape of the MFS. A graphic illustration of these quantities is also given, where possible, in Figure 9.

Let us start with  $\alpha_0$ , namely the abscissa of the MFS peak: it is lower if the signal is uncorrelated and the underlying process “loses fine structure”, i.e. the dominant fractal structure has more signal at larger fluctuations, since fine fluctuations become less frequent, so the object becomes more regular in appearance. In Table 2 a systematic increase<sup>7</sup> is seen for  $\alpha_0$  from 70 to  $500 \mu\text{m}$  for any Hi-GAL tile. In particular, the largest gaps are seen between 70 and  $160 \mu\text{m}$ , and from  $160 \mu\text{m}$  to SPIRE wavelengths, while the column density maps show  $\alpha_0$  values close to those of the SPIRE maps, with no correspondence to a particular wavelength. The observed behaviour can be ascribed to the increasing degree of “structure” at increasing wavelength, namely a gradual enhancement of diffuse emission compared to isolated strong singularities. Furthermore, the most quiescent single tiles ( $\ell 215, \ell 220$ ) show lower  $\alpha_0$  compared to the others; in particular, at SPIRE wavelengths, they are characterized by  $\alpha_0 < 2.015$ , while  $\alpha_0 > 2.020$  for the remaining tiles. No systematic trends are found, instead, among different simulations

<sup>7</sup> The differences among  $\alpha_0$  values are generally found on the second or the third decimal digit (for this reason the precision of the  $\alpha_0$  values quoted in Tables 2, 3, and 4 is increased with respect to other analogous parameters). Despite this, they show interesting systematic trends.

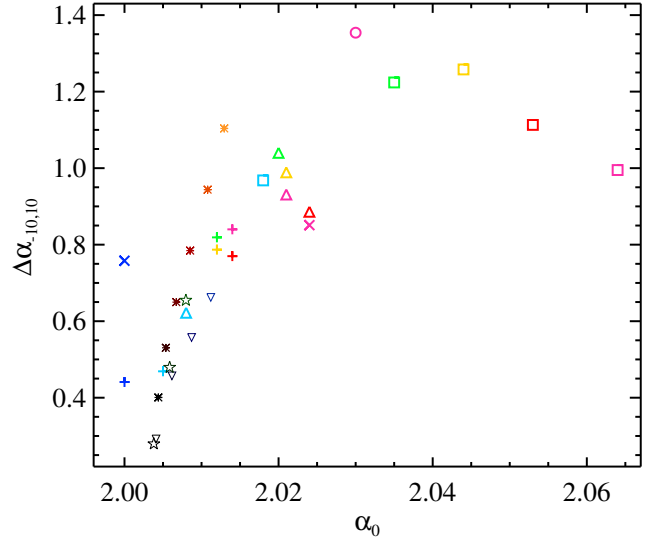


**Figure 10.** Plot of the MFS “amplitude”  $\Delta\alpha_{-10,10}$  versus the peak position  $\alpha_0$  for the maps studied in this work for which a reliable  $\alpha$  values in the the  $10 \leq q \leq 10$  range was derived. Data corresponding to the three turbulent ISM simulations with available  $\Delta\alpha_{-10,10}$  (see Table 3) are all located at  $\alpha_0 > 2.1$  and  $\Delta\alpha_{-10,10} > 2.2$  and are not displayed here not to overly compress the plot. The symbols are the same introduced in the legend of Figure 8.

(Table 3), except the remarkably large  $\alpha_0$  values for the “compressive forcing” case, corresponding to a significantly more correlated signal, as already found, with respect to the “solenoidal forcing” case, by Federrath et al. (2009) through the structure function analysis. Finally, a little but systematic increase of  $\alpha_0$  at increasing  $\beta$  is seen for the fBm images (Table 4); notice indeed that for this class of objects, starting from the case  $\beta = 0$  (white noise), corresponding to a totally uncorrelated signal, correlation increases with increasing  $\beta$ .

#### 4.2.3 MFS width

A second relevant quantity is the MFS width, which expresses the degree of multifractality of the investigated set. The wider the range, the more multifractal are the fluctuations in the image. We express it here through the  $\Delta\alpha_{-10,10} \equiv \alpha_{-10} - \alpha_{10}$  parameter (see, e.g., Macek 2007). In Figure 10, this quantity is plotted versus  $\alpha_0$  for those maps having a MFS not involving cusps in  $-10 \leq q \leq 10$ . The considerations written above about  $\alpha_0$  are easily recognizable in the abscissae of the points in the plot but, in addition, an interesting trend is seen between the two plotted quantities, with the degree of multifractality  $\Delta\alpha_{-10,10}$  generally increasing at increasing degree of complexity expressed by  $\alpha_0$ . Such a trend is more easily recognizable for fBm images at increasing  $\beta$ , although confined to a shorter range of  $\alpha_0$ , than for Hi-GAL maps, whose corresponding points are more scattered.

Another way to measure the amplitude of a MFS is to compute the area  $A_\Phi$  delimited by the MFS curve and a given horizontal cut at a level  $f = \Phi$ :

$$A_\Phi = \int_{\alpha_{\Phi,1}}^{\alpha_{\Phi,2}} [f(\alpha) - \Phi] d\alpha, \quad (15)$$

where  $\alpha_{\Phi,1}$  and  $\alpha_{\Phi,2}$  represent the abscissae of the two points of the MFS for which  $f = \Phi$ . The area  $A_\Phi$ , illustrated in Figure 9 as a grey

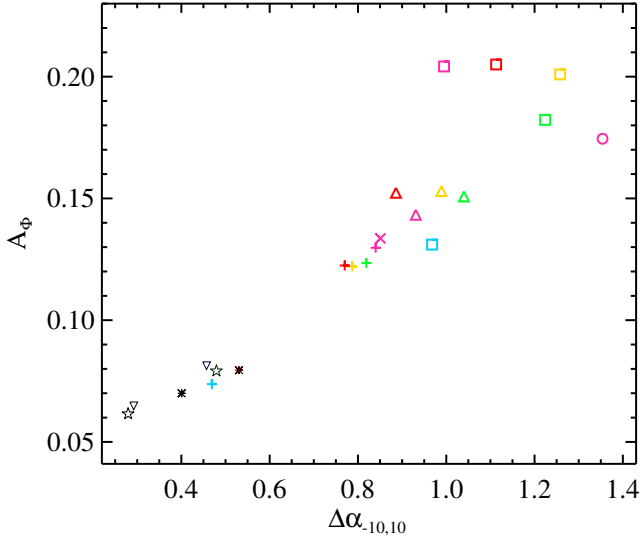


**Figure 11.** Plot of the area  $A_\Phi$  under the MFS and above  $f = 1.5$  versus  $\Delta\alpha_{-10,10}$  for maps for which both quantities can be derived. The symbols are the same introduced in the legend of Figure 8.

region, can be evaluated only for MFSs whose left and right tails are both intersected by the cut at  $f = \Phi$ , which is formally expressed by the condition  $\alpha_{\min} < \alpha_{\Phi,1} < \alpha_{\Phi,2} < \alpha_{\max}$ . This also accounts for the presence of possible cusp-like behaviour in the spectrum. The  $A_\Phi$  obtained (choosing  $\Phi = 1.5$ ) for Hi-GAL fields, fBm sets and simulations are quoted in Tables 2, 3, and 4, respectively.

The correlation between  $A_\Phi$  and  $\Delta\alpha_{-10,10}$  is investigated in Figure 11, displaying a roughly linear correlation between these two descriptors, as expected, since an increase of the MFS width should correspond to an increase of  $A_\Phi$ , being the ordinate of the MFS peak constant. Larger departures from this behaviour are seen at large values of these quantities, especially for  $350 \mu\text{m}$ ,  $500 \mu\text{m}$  and column density images of  $\ell 224$ . This indicates a particularly “swollen” shape of MFS, quite well recognisable in the  $\ell 224$  panel of Figure 5, especially for the column density map. As in the case of Figure 10, in Figure 11 the points corresponding to simulations (three available cases: #5, #6, and #9 of Table 3) are not shown, being all of them located at  $\Delta\alpha_{-10,10} > 2.2$  and  $A_\Phi > 0.3$ , that is to say far from the region of the plot populated by observational data sets, highlighting a different structure compared with real data. In particular, since both  $\Delta\alpha_{-10,10}$  and  $A_\Phi$  are descriptors of the degree of multifractality in the signal, this indicates a generally wider variety of structures than observed in Hi-GAL tiles.

In our case, the benefit of using  $A_\Phi$  instead of  $\Delta\alpha_{-10,10}$  to represent the MFS amplitudes consists of a larger number of useful maps. In Figure 12 the  $A_\Phi$  versus  $\alpha_0$  plot confirms, based on a larger sample of cases, the trends seen in Figure 10. The plot appears less scattered than that of Figure 10 with regard to positions of Hi-GAL and fBm images, while the positions of the simulations cover a wide range towards larger values. The “solenoidal” and the  $t_1, yz$  maps of both the “quasi-hydrodynamical” and “high magnetization” scenarios are the closest to the observational points, mostly to the ones corresponding to SPIRE maps of  $\ell 224$  and  $\ell 217$ , that is to say that, from the point of view of the MFS amplitude, they show a degree of multifractality similar to that of the most actively star forming regions in our sample.

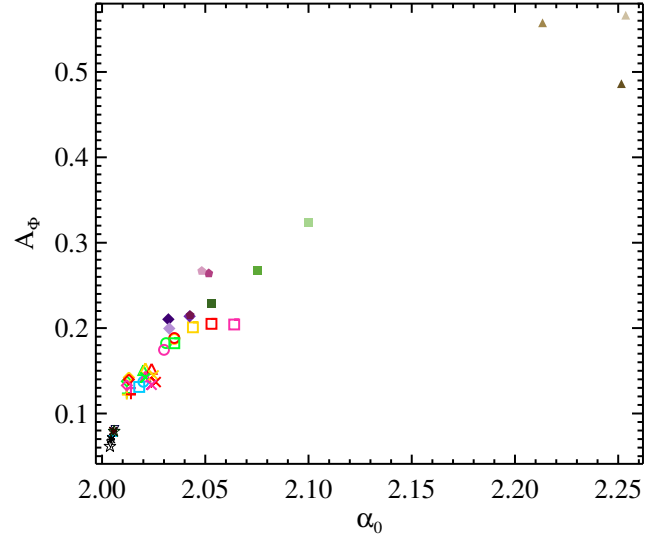


**Figure 12.** Plot of the area  $A_\Phi$  under the MFS and above  $f = 1.5$  versus the peak position  $\alpha_0$  for maps for which  $A_\Phi$  can be derived. The symbols are the same introduced in the legend of Figure 8.

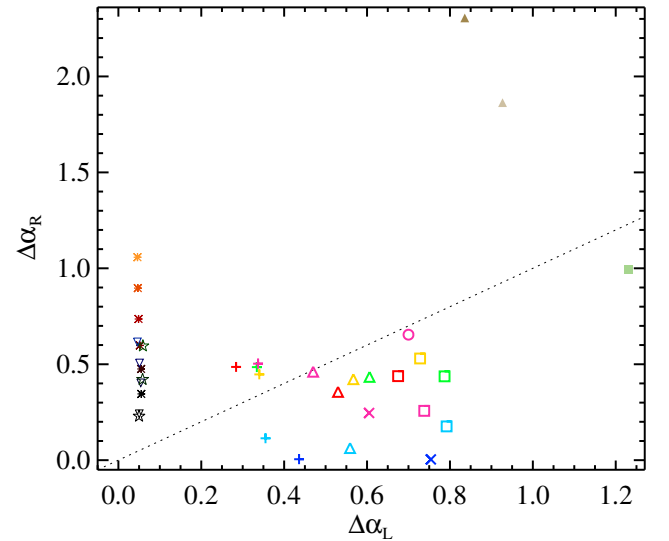


**Figure 13.** Plot of the MFS left versus right tail amplitude for maps for which it is possible to derive both quantities. The symbols are the same introduced in the legend of Figure 8. The dotted line represents the bisector, to facilitate the distinction between left-skewed (below the line) and right-skewed (above the line) MFSs, respectively.

#### 4.2.4 Left vs right tail width

The diagnostics used in Figures 10, 11, and 12 consider the MFS as a whole, neglecting information contained in possible asymmetries. In fact, the left tail of the MFS represents the heterogeneity (broad tail) or uniformity (narrow tail) of the high values distribution, as well as the right tail is related to heterogeneity/uniformity of the low values distribution (e.g., Pavon-Dominguez et al. 2013; de Freitas et al. 2017). Strong asymmetries are observed in most of the spectra analysed in this paper, with the extreme case represented by PACS  $70 \mu\text{m}$  maps, discussed above.

In order to make use of the MFS asymmetry, single values of  $\alpha$  on the two sides of the MFS (for example,  $\alpha_{10}$  and  $\alpha_{-10}$ ,



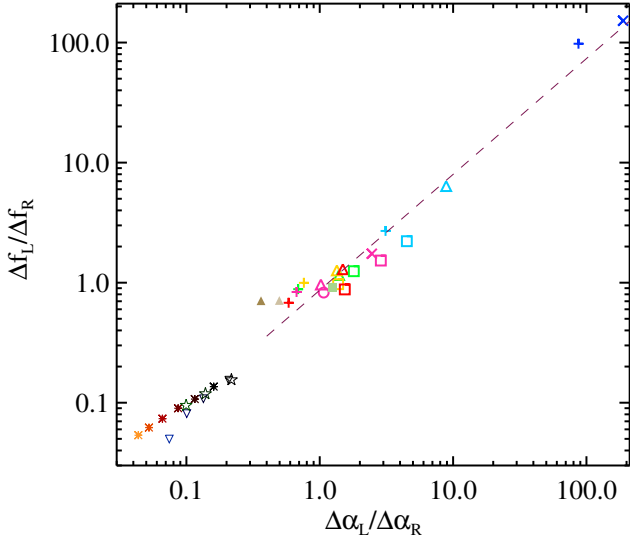


**Figure 14.** Plot of the MFS vertical versus horizontal balance (estimated involving orders  $q = -10, 10$ ) for maps for which it is possible to derive both quantities. The symbols are the same introduced in the legend of Figure 8. The grey dashed line represents the power-law best fit to the locii of the Hi-GAL maps.

to follow the same approach as above) should be considered (de Freitas et al. 2017). In Figure 13 the two widths  $\Delta\alpha_L \equiv \alpha_{-10} - \alpha_0$  and  $\Delta\alpha_R \equiv \alpha_{-10} - \alpha_0$ , are plotted. First, a strong segregation in abscissa is visible between the group of fBm sets (which are right-skewed and for which the width of the left MFS tail  $\alpha_{10}$  remains nearly constant, see also Table 3) and that of Hi-GAL maps. The latter is internally more composite: the most quiescent,  $\ell 215$ , is found on the left while the most active,  $\ell 224$ , on the right, as a consequence of the leftward broadening of the MFS in presence of bright compact sources (cf. Figure 5). Along the vertical coordinate, a systematic increase is seen from short to long *Herschel* wavelengths, while the column density maps appear mixed with SPIRE maps but with no specific trend.

For the fBm images, the increase of  $\Delta\alpha_R$  at increasing  $\beta$  corresponds to the progressive rightward broadening of the MFS seen in Figure 7.

About the simulations, as in Figure 11 only three cases (with a MFS very different in general from that of observations) survive the constraint of absence of possible cusps, and populate a very different plot region, with both coordinates larger than those of observations. The lack of other nine cases prevents us from completing here quantitatively the qualitative description of Figure 6. We postpone the analysis of implications of the physics contained in the models to Section 4.3, in which an equivalent approach, but in terms of generalised fractal dimension, is discussed.

#### 4.2.5 Vertical vs horizontal balance

The degree of asymmetry of a MFS can be expressed by the ratio between the left and right tail widths  $\Delta\alpha_L/\Delta\alpha_R$  (e.g., Drożdż & Oświęcimka 2015; de Freitas et al. 2017), with a left-skewed spectrum corresponding to the dominance of extreme events, and a right-skewed one denoting relatively strongly weighted high fractal exponents, which correspond to fine structures (e.g., Krzyszczak et al. 2017). In order to capture the general proportions of the MFS, this horizontal balance can be analysed jointly with the

vertical one based on the extents along the  $f$  direction, namely  $\Delta f_L/\Delta f_R \equiv (f_0 - f_{10})/(f_0 - f_{-10})$ . For example, an increase of the “fractal divergence” numerator  $\Delta f_L$  is shown by destruction of uniformity into a wide range of fractal dimensionality. The vertical versus horizontal balance plot for the available MFSs is shown in Figure 14, in which a direct correlation between the two is seen, in general. This implies that an asymmetry in the MFS is typically composed by the predominance of a tail of the spectrum on the other one both in width and in total vertical extent. However, in this general trend different sub-regions can be easily recognised: in the left-bottom part of the diagram ( $\Delta\alpha_L/\Delta\alpha_R < 0.2, \Delta f_L/\Delta f_R < 0.2$ ) the fBm images are located, as a consequence of their strongly right-skewed MFS. On the contrary, the SPIRE and column density Hi-GAL fields are found to be mildly right-skewed ( $\ell 215$ ) or left-skewed ( $\ell 217, \ell 222, \ell 224$ ). The PACS 160  $\mu\text{m}$  maps populate the right-top of this group, while the 70  $\mu\text{m}$  maps are located very far, at the top right end of the diagram, due to the disproportion between the left and the right branch of the MFS in these cases. The trend followed by the Hi-GAL maps can be fitted to a power-law relation, with  $\Delta f_L/\Delta f_R = (0.87 \pm 0.07) \times (\Delta\alpha_L/\Delta\alpha_R)^{(0.96 \pm 0.04)}$ , i.e. an almost linear behaviour. Finally, two out of the three displayed models show a departure from the typical behaviour of the observational ISM maps, being located at lower values of  $\Delta\alpha_L/\Delta\alpha_R$ .

One of the main goals of this work is to show how the extension of the multifractal analysis of the ISM to negative  $q$  orders permits a more refined classification of the images through their MFS. The tools used to produce Figures 10 to 14 confirm that the ISM maps show common trends as the one revealed in Figure 8 only based on the positive  $q$  portion of the MFS. However they reveal further relations (e.g., the behaviour of the peak position, the peculiarities of the PACS maps, the differences between observational and simulated maps, etc.) as well, which represent new useful tools we suggest for a thorough statistical analysis of ISM maps.

### 4.3 Generalised fractal dimension approach

In this section, the alternative view provided by the generalised fractal dimension approach is presented. On the one hand, since this representation is practically equivalent to the MFS one through Equations 8 and 9, we will not comment in detail the behaviour of  $D_q$ , but mostly and briefly highlight how features found with this approach are already recognisable in the MFS. On the other hand, this approach permits a more direct and intuitive comparison with the mono-fractal properties of the investigated sets.

In Figure 15 the  $D_q$  curves are shown for each Hi-GAL tile and each band (plus the column density maps), to facilitate the recognition of possible common trends. The most evident features are:

- A clear asymmetry is found for all curves between the negative and the positive  $q$  regions (concave upward in the former, and downward in the latter). Its extent mirrors the degree of asymmetry typically found for these maps between the right and the left part of the MFS.
- The maps at 70  $\mu\text{m}$  show in all cases a peculiar behaviour: for  $q < 0$ ,  $D_q$  is practically constant around  $\approx 2$ , which corresponds to an uniform plus random noise distribution. This is seen also in the MFS analysis as an extremely short right tail of the MFS (cf. Figure 5). In contrast, these maps can exhibit very bright concentrations of emission corresponding to star forming objects/regions, which are enhanced by the  $q > 0$  analysis. In fact, mainly for the tiles with the highest content of star formation, namely  $\ell 217$  and

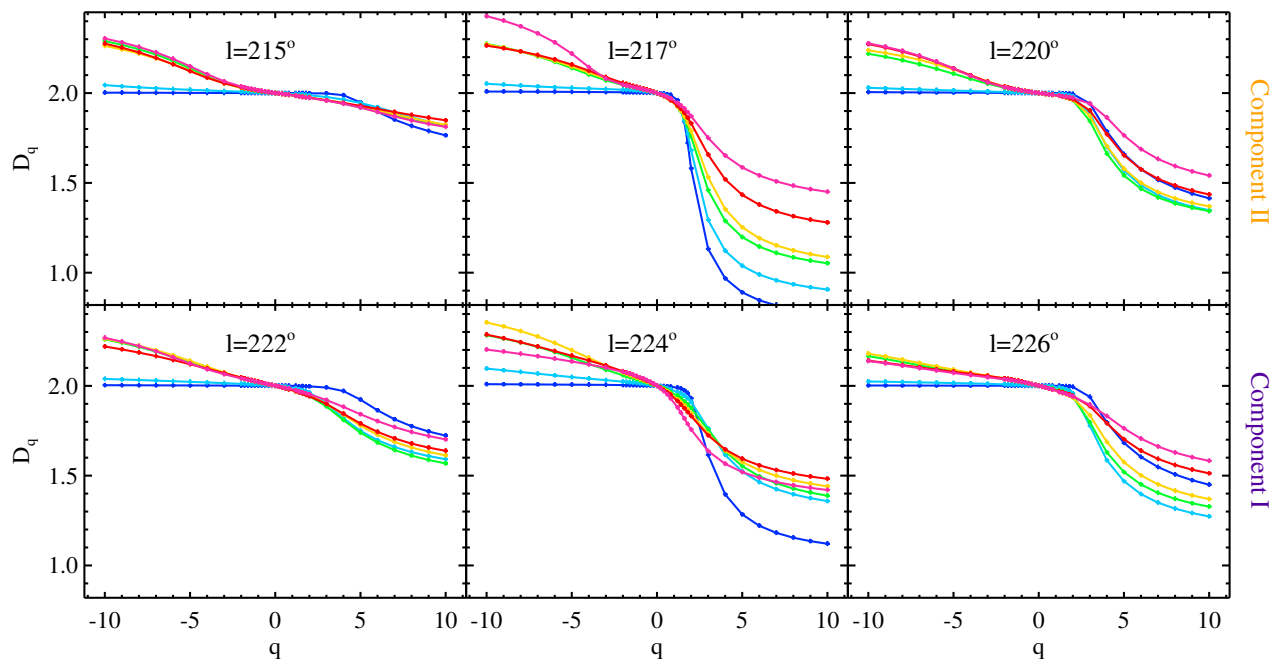


**Figure 15.** Generalised fractal dimension  $D_q$  versus order  $q$  for the Hi-GAL maps analysed in this work, ordered by tile and color-coded as in Figure 5.

$\ell 224$ , the scaling of  $D_q$  is far from being constant and, instead, the  $70 \mu\text{m}$  band shows the largest departures from the typical value of 2, reaching  $D_q < 1$  in the case of  $\ell 217$ . This corresponds to the enlarged left tails of the MFS observed for these two tiles at this band.

- As seen also for the MFS, the maps at  $160 \mu\text{m}$  show a behaviour which is intermediate between that of the  $70 \mu\text{m}$  and that of the SPIRE (and column density) ones, which, in turn, show a more similar behaviour among them.
- The tiles  $\ell 217$  and  $\ell 224$  show the largest differences, not only at  $70 \mu\text{m}$  (as pointed out above) between fractal dimensions of negative and positive orders, and this indicates a remarkable departure from a simple fractal behaviour.

Concerning the last point, it is interesting to explore how a mono-fractal indicator, such as the fractal dimension estimated as in Paper I, is correlated with the generalised fractal dimensions estimated here. To do this, the fractal dimensions have been derived for the  $\ell 215$  and  $\ell 226$  Hi-GAL maps, not included in Paper I, as well as for the remaining tiles because of their different size (see Section 2.1). In Appendix C the method used to calculate the fractal dimension  $D_\Delta$  for all tiles at all wavelengths through the  $\Delta$ -variance technique is described, and the obtained values are reported (Table C1). We use these values to build Figure 16, in which  $D_{-10}$  and  $D_{10}$  are plotted versus  $D_\Delta$  (top and bottom panel, respectively), as representative cases of negative and positive  $q$  dimensions, respectively. First, some considerations are in order about the distribution of  $D_\Delta$ : in Paper I it was found that, inside a given component, tiles rich in star forming regions ( $\ell 224$  for component I and  $\ell 217$  for component II, respectively) generally show, at each band, a larger  $D_\Delta$  than those containing more quiescent ISM (with a unique exception given by the fractal dimension of the column density map of  $\ell 222$ , larger than that of  $\ell 224$ ). Here

this behaviour is confirmed<sup>8</sup> by the high  $D_\Delta$  found for the active field  $\ell 226$  (component I) and, on the opposite side, for the low ones found for the low-emission field  $\ell 215$  (component II). This trend is mixed with another one consisting in a systematic decrease (from very evident for  $\ell 224$  to practically absent for  $\ell 222$ ) of  $D_\Delta$  with wavelength from  $160$  to  $500 \mu\text{m}$ .

That being said, the plot of  $D_{-10}$  versus  $D_\Delta$  shows no correlation between these two dimensions, being the former relatively well confined:  $D_{-10} \lesssim 2.1$  for maps at  $160 \mu\text{m}$  and  $2.1 \lesssim D_{-10} \lesssim 2.45$  for SPIRE and column density maps. Instead, the  $D_{10}$  dimension shows a linearly decreasing trend at increasing  $D_\Delta$ , which can be represented by a linear fit:  $D_{10} = (3.92 \pm 0.21) - (0.86 \pm 0.07) \times D_\Delta$ . In practice, this highlights that, at least for the investigated Hi-GAL fields, the mono-fractal dimension is mostly sensitive to the scaling of large fluctuations and strong singularities.

To complete this comparative analysis, we also examine the behaviour of  $D_q$  vs  $q$  also for the simulated column density maps and the fBm sets considered in this paper (Figures 17 and 18, respectively).

In the case of simulations, arguments similar to those emerging from the MFS analysis can be repeated: the elongation of  $D_q$  values, both at  $q < 0$  and  $q > 0$ , in the “compressive forcing” case is larger than in the “solenoidal forcing” one (Figure 17, top panels), connected to the fact that the MFS is found to be broader. The very low  $D_q$  values at positive  $q$  orders for the maps corresponding to the  $t_2$  epochs for the “quasi-hydrodynamical” and “high-magnetization” scenarios (Figure 17, bottom panels) are parallel to the broadening of the MFS left tail as a consequence of the increase of star forming activity in these simulations.

The fBm images show a strong divergence between the negative  $q$  portion of the  $D_q$  curve, which gets higher as  $q$  decreases or  $\beta$  increases, and the positive  $q$  one, in which differences between

<sup>8</sup> See Appendix C for the discussion of the consistency between  $D_\Delta$  values obtained in this work and in Paper I for the tiles in common.

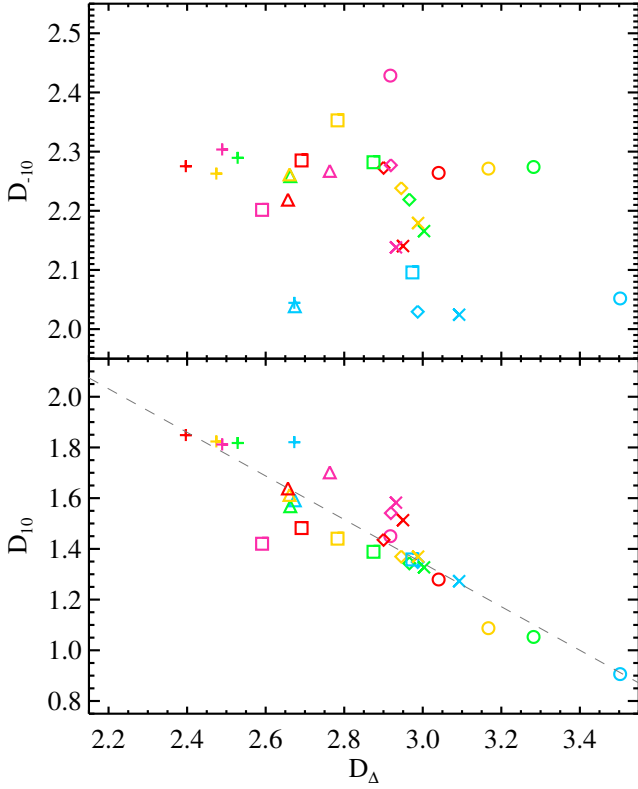


**Figure 16.** Plot of the fractal dimensions of order  $q = -10$  (top panel) and 10 (bottom panel) versus the mono-fractal dimension  $D_{\Delta}$  estimated through the  $\Delta$ -variance technique (see Appendix C) for the six Hi-GAL fields studied in this paper. Symbols and colors are the same coded in Figure 8, with the addition of the  $\ell 226$  maps, indicated with an asterisk. The  $70 \mu\text{m}$  maps are not shown, being  $D_{\Delta}$  unreliable for these maps (see Paper I).

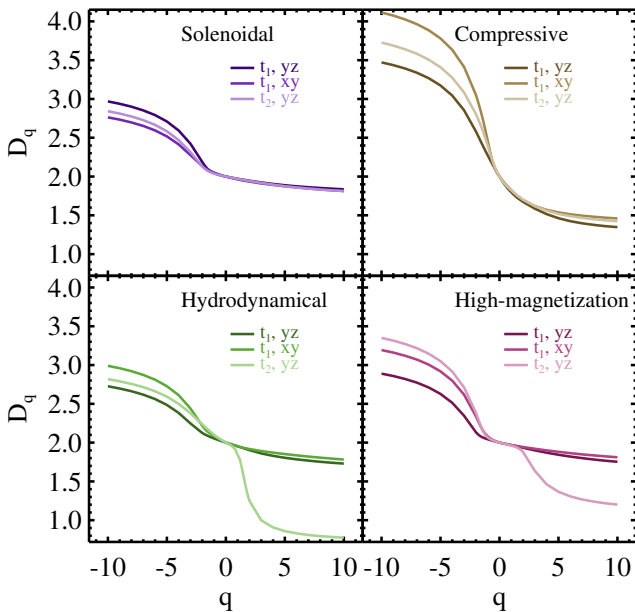


**Figure 17.** Generalised fractal dimension  $D_q$  versus order  $q$  for the column density maps produced by the numerical simulations analysed in this work, arranged by model and color-coded as in Figure 6.

images at different  $\beta$  are much smaller (although still systematic). Again, this effect corresponds to the strong broadening of the right tail of the MFS, with respect to the left one, observed at increasing  $\beta$  (Figure 7).

On the basis of the above considerations, a plot based on salient features of the  $D_q$  curves should not add new information with respect to the analysis in Section 4.2 using the main features of the MFS. Nevertheless, since the  $D_q$  curves are not affected by features like the cusps appearing in some MFS, there is no limitation, for example, in displaying the  $D_{20}$  versus  $D_{-10}$  for all the investigated maps, as a measure of the excursion between values found at the extreme positive and negative probed orders  $q$  (Figure 19). The three classes of images populate different zones of the diagram:

- The Hi-GAL images occupy a vertical belt delimited by  $2.0 \leq D_{-10} \leq 2.4$ , in which, from left to right, the PACS maps are encountered before the SPIRE and column density ones. At the top of the group, the  $\ell 215$  and  $\ell 222$  maps are found, i.e. the most quiescent fields, while the  $\ell 217$  maps represent the bottom of the population.
- The numerical simulations occupy a wide region of the plot at  $D_{-10} \geq 2.7$ , in which it is possible to distinguish two further sub-groups: (i) seven maps on the top ( $D_{20} > 1.6$ ) including the three of the “solenoidal” case, and the maps (on both projections) at  $t_1$  of the “quasi-hydrodynamical” and “high-magnetization” cases, and (ii) five maps at lower  $D_{20}$  including the three of the “compressive forcing” case, and the maps at  $t_2$  of the “quasi-hydrodynamical” and “high-magnetization” cases. The seven maps of the group *i* correspond to statistically similar structure, shaped by pure turbulence. When gravity, absent in the evolution of the “solenoidal” scenario, becomes predominant at  $t_2$  in the “quasi-hydrodynamical” and “high-magnetization” cases,  $D_{20}$  decreases, more significantly in the first case, in absence of magnetic support of the cloud (see Appendix B for a more systematic analysis of the effects of gravity and magnetic field).
- A narrow horizontal belt at  $D_{20} = 1.95$  populated by fBm images, being the low- $\beta$  on the left and the high- $\beta$  on the right.

Figure 19 summarizes some of the main results of our analysis: at least for our choice of observations and simulations, the multifractal behaviour of the former and of the latter appear quite different, despite the wide range of physical conditions explored. Qualitatively speaking, common behaviours can be recognised, such as the decrease of  $D_{20}$  (or, correspondingly, the broadening of the left tail of the MFS) as the star forming content increases, but from the quantitative point of view the typical values of generalised fractal dimensions remain remarkably different, so that a clear segregation of image classes is found. The fBm images denote again a different behaviour with respect to the other two classes, and, in the light of the multifractal analysis, seem inadequate to be representative of the statistical properties of ISM, contrarily to what the mono-fractal analysis typically suggests.

## 5 CONCLUSIONS

The need of extending the multifractal description of the ISM, so far attempted only by Chappell & Scalo (2001), to more recent, high-quality, and statistically meaningful data motivated this work. We carried out the multifractal analysis of six Hi-GAL fields in a region of the third Galactic quadrant already described by Elia et al. (2013), and characterised by a conveniently low degree of velocity component overlap along the line of sight. These fields are

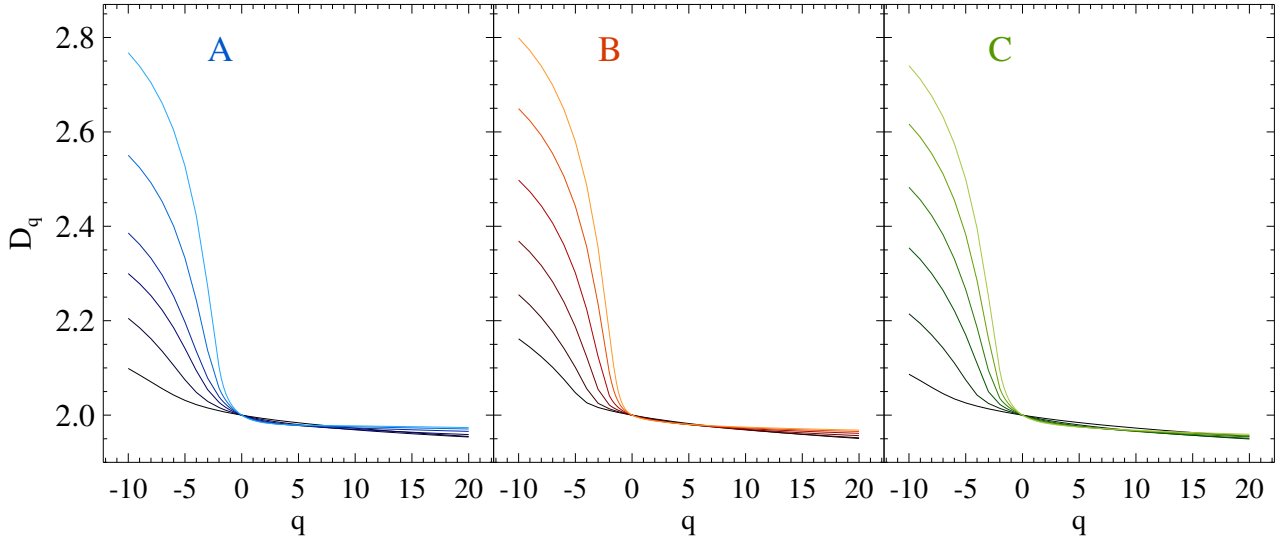


**Figure 18.** Generalised fractal dimension  $D_q$  versus order  $q$  for the fBm images analysed in this work, grouped by common phase distribution and color-coded as in Figure 4 (from dark to light as the power spectrum exponent  $\beta$  increases from 2 to 4 in steps of 0.4).

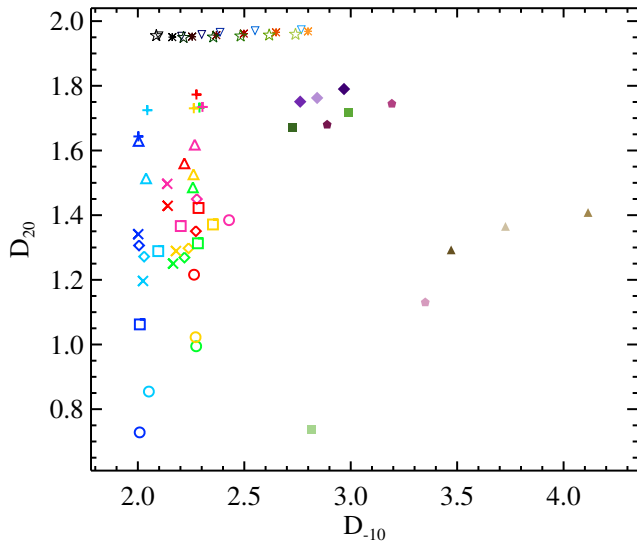


**Figure 19.** Fractal dimension of order  $q = 20$  versus the one of order  $q = -10$  for all the maps analysed in this paper. Symbols and colors are the same introduced in Figure 8.

interesting by themselves, thanks to the variety of morphologies and physical conditions displayed by the ISM in this region.

For comparison, the same analysis was extended to 30 synthetic maps: 12 column density maps of simulated clouds extracted from the STARFORMAT data base and obtained from four different numerical models, at two projections and two evolutionary epochs, and 18 fBm sets spanning a variety of power spectrum slopes and initial phase distributions.

A number of results emerged from this analysis. The most important ones are summarised as follows:

(i) All the investigated fields exhibit a multifractal rather than a simple monofractal structure. The variety of the obtained MFS shapes permits a further differentiation among them.

(ii) Strong differences are found between the left and the right tail of the MFS. Most of the analysed Hi-GAL maps exhibit a broader

left tail of the MFS with respect to the right one, with the extreme case of the  $70 \mu\text{m}$  maps, presenting a right tail almost collapsed to a single point against a pronounced left one, signature of the presence of several bright spots on a very low-signal background, as the maps at this wavelength typically appear in this portion of the Galaxy.

(iii) The roughly linear relation between the strength of the brightest singularities and dimensional diversity in the ISM maps found by Chappell & Scalo (2001) is confirmed by our analysis of Hi-GAL fields at various wavelengths.

(iv) The peak position and the total width of the MFS appear to systematically drift, for a given tile, with wavelength, denoting an increase of image complexity at increasing wavelength due to the progressive appearance of a network of filaments and of cold structures in general. Moreover, global behaviours are recognisable from tile to tile, from star formation-rich to more quiescent ones (more and less “complex”, respectively).

(v) The MFS of the Hi-GAL fields is generally left-skewed, with the exception of the  $\ell 215$  tile. This is mostly associated to a lower  $f$  initial value for the predominant tail with respect to the opposite extreme of the MFS, so that the “vertical” versus “horizontal balance” of the MFS appear to follow a direct power law with exponent close to 1.

(vi) Comparing the generalised fractal dimensions of the Hi-GAL maps with the mono-fractal ones, a clear correlation is seen at positive orders (nearly linear at  $q = 10$ ), suggesting that the estimates of the fractal dimension are strongly influenced by the strongest brightness peaks present in the maps.

(vii) The cloud models partly exhibit different behaviours, depending on the underlying physics. The “compressive forcing” maps show a different MFS compared to observations. The “solenoidal forcing”, “quasi-hydrodynamical”, and “high-magnetization” show relatively similar spectra at the earliest of the two considered epochs (with small differences among different projections), but with the last two presenting a systematic broadening of the left tail of the MFS as their star formation content increases under gravity action, in agreement with the behaviour recognised for observational maps. The presence of a magnetic support of the cloud, instead, is seen to contrast this effect

(viii) Despite qualitative similarities between the MFS derived

for observed maps and numerical simulations, using quantitative descriptors of the MFS shape (such as peak position, spectrum width and skewness, etc.) a segregation between the two image classes is found. This is also emphasized by the analysis of the generalised fractal dimension, suggesting that, at least for the analysed set of maps, simulations do not completely fulfill the constraints on the structure suggested by the multifractal analysis of observational maps.

(ix) The multifractal analysis of fBm images reveals that they show a remarkably different behaviour compared with our observed maps, suggesting that, despite analogies between power spectra, the Fourier phase distributions for these two classes can be quite different and responsible of the observed discrepancies. All the used indicators advise against the use of the fBm images as a surrogate for the observations.

Moreover, this study has produced some interesting results about fBm images by themselves, of interdisciplinary relevance independently from the comparison with observations:

(x) The increase of the power spectrum exponent  $\beta$  generally produces a rise of the last point of the left part of the MFS and a strong systematic enlargement of the right tail of the MFS. The peak position increases as well at increasing  $\beta$ .

(xi) On the other hand, the MFSs of two fBm generated with the same  $\beta$  and a different random phase distribution, are not identical although they have the same fractal dimension. This represents a further evidence of the general importance of analysing the Fourier phases together with the simple power spectrum.

Possible extension of this work will consist in enlarging the sample of analysed *Herschel* fields, provided that they are associated to a predominant gas velocity component, as well as the number of the considered models, searching for possible points of contact of the two classes that could have been missed in the present analysis.

## ACKNOWLEDGEMENTS

NS acknowledges support by the French ANR and the German DFG through the project “GENESIS” (ANR-16-CE92-0035-01/DFG1591/2-1). ES acknowledges support from the EU-funded VIALACTEA programme (FP7-SPACE-607380607380). *Herschel* is an ESA space observatory with science instruments provided by European-led Principal Investigator consortia and with important participation from NASA.

## REFERENCES

Abry P., Jaffard S., Lashermes B., 2004, in Truchetet F., Laligant O., eds, Proc. SPIE Vol. 5607, Wavelet Applications in Industrial Processing II, pp 103–117, doi:10.1117/12.581234

Arneodo A., Bacry E., Muzy J. F., 1995, *Physica A Statistical Mechanics and its Applications*, 213, 232

Bensch F., Stutzki J., Ossenkopf V., 2001, *A&A*, 366, 636

Borgani S., Murante G., Provenzale A., Valdarnini R., 1993, *Phys. Rev. E*, 47, 3879

Burkhart B., Lazarian A., 2016, *ApJ*, 827, 26

Burkhart B., Lazarian A., Goodman A., Rosolowsky E., 2013, *ApJ*, 770, 141

Burkhart B., Stalpes K., Collins D. C., 2017, *ApJ*, 834, L1

Burton M. G., et al., 2013, *Publ. Astron. Soc. Australia*, 30, e044

Cadavid A. C., Rivera Y. J., Lawrence J. K., Christian D. J., Jennings P. J., Rappazzo A. F., 2016, *ApJ*, 831, 186

Chappell D., Scalo J., 2001, *ApJ*, 551, 712

Chhabra A., Jensen R. V., 1989, *Physical Review Letters*, 62, 1327

Dib S., Burkert A., 2005, *ApJ*, 630, 238

Dib S., Hennebelle P., Pineda J. E., Csengeri T., Bontemps S., Audit E., Goodman A. A., 2010, *ApJ*, 723, 425

Drożdż S., Oświęcimka P., 2015, *Phys. Rev. E*, 91, 030902

Dubey A., et al., 2008, in Pogorelov N. V., Audit E., Zank G. P., eds, *Astronomical Society of the Pacific Conference Series Vol. 385, Numerical Modeling of Space Plasma Flows*. p. 145

Elia D., et al., 2013, *ApJ*, 772, 45

Elia D., et al., 2014, *ApJ*, 788, 3

Elmegreen B. G., 1995, in Pena M., Kurtz S., eds, *Revista Mexicana de Astronomia y Astrofísica*, vol. 27 Vol. 3, *Revista Mexicana de Astronomia y Astrofísica Conference Series*. p. 289

Elmegreen B. G., Falgarone E., 1996, *ApJ*, 471, 816

Elmegreen B. G., Scalo J., 2004, *ARA&A*, 42, 211

Falconer K., 2003, *Fractal Geometry - Mathematical Foundations and Applications 2e: Mathematical Foundations and Applications*. Wiley, Chichester, <https://cds.cern.ch/record/1250049>

Falgarone E., Hily-Blant P., Levrier F., 2004, *Ap&SS*, 292, 89

Federrath C., Klessen R. S., Schmidt W., 2008, *ApJ*, 688, L79

Federrath C., Klessen R. S., Schmidt W., 2009, *ApJ*, 692, 364

Federrath C., Roman-Duval J., Klessen R. S., Schmidt W., Mac Low M.-M., 2010, *A&A*, 512, A81

Fromang S., Hennebelle P., Teyssier R., 2006, *A&A*, 457, 371

Fryxell B., et al., 2000, *ApJS*, 131, 273

Griffin M. J., et al., 2010, *A&A*, 518, L3

Gu G.-F., Zhou W.-X., 2006, *Phys. Rev. E*, 74, 061104

Halsey T. C., Jensen M. H., Kadanoff L. P., Procaccia I., Shraiman B. I., 1986, *Phys. Rev. A*, 33, 1141

Hennebelle P., 2018, *A&A*, 611, A24

Hentschel H. G. E., Procaccia I., 1983, *Phys. Rev. A*, 27, 1266

Jackson J. M., et al., 2006, *ApJS*, 163, 145

Khalil A., Joncas G., Nekka F., Kestener P., Arneodo A., 2006, *ApJS*, 165, 512

Kowal G., Lazarian A., Beresnyak A., 2007, *ApJ*, 658, 423

Kritsuk A. G., Norman M. L., Padoan P., Wagner R., 2007, *ApJ*, 665, 416

Krumholz M. R., 2014, *Phys. Rep.*, 539, 49

Krzyszczak J., Baranowski P., Zubik M., Hoffmann H., 2017, *Agricultural and Forest Meteorology*, 239, 223

Lou D., Zhang C., Liu H., 2015, *Journal of Geochemical Exploration*, 157, 169

Lutz D., 2012

Macek W. M., 2007, *Nonlinear Processes in Geophysics*, 14, 695

Mandelbrot B., 1967, *Science*, 156, 636

Mandelbrot B. B., 1989, in Mezzetti M., Giuricin G., Mardirossian F., Ramella M., eds, *Astrophysics and Space Science Library Vol. 151, Large Scale Structure and Motions in the Universe*. pp 259–278, doi:10.1007/978-94-009-0903-8\_19

Maruyama F., Kai K., Morimoto H., 2017, *Advances in Space Research*, 60, 1363

Meneveau C., Sreenivasan K. R., 1987, *Physical Review Letters*, 59, 1424

Meredith D. C., Ryan J. M., Young C. A., 1995, *Ap&SS*, 231, 111

Miville-Deschênes M.-A., Levrier F., Falgarone E., 2003, *ApJ*, 593, 831

Mocz P., Burkhart B., Hernquist L., McKee C. F., Springel V., 2017, *ApJ*, 838, 40

Molinari S., et al., 2010, *PASP*, 122, 314

Molinari S., et al., 2016, *A&A*, 591, A149

Movahed M. S., Ghasemi F., Rahvar S., Tabar M. R. R., 2011, *Phys. Rev. E*, 84, 021103

Onishi T., Mizuno N., Mizuno A., Fukui Y., Nanten Team 2005, in *Protostars and Planets V Posters*. p. 8301

Pan J., Coles P., 2000, *MNRAS*, 318, L51

Pavon-Dominguez P., Jimenez-Hornero F. J., de Rave E. G., 2013, *Atmospheric Pollution Research*, 4, 229

Peitgen H.-O., Saupe D., eds, 1988, *The Science of Fractal Images*. Springer-Verlag New York, Inc., New York, NY, USA

Pfenniger D., 1996, in Block D. L., Greenberg J. M., eds, *Astrophysics*



- and Space Science Library Vol. 209, New Extragalactic Perspectives in the New South Africa. p. 439 (arXiv:astro-ph/9602144), doi:10.1007/978-94-009-0335-7\_53
- Pilbratt G. L., et al., 2010, *A&A*, 518, L1
- Poglitsch A., et al., 2010, *A&A*, 518, L2
- Scalo J., 1990, in Capuzzo-Dolcetta R., Chiosi C., di Fazio A., eds, *Astrophysics and Space Science Library* Vol. 162, *Physical Processes in Fragmentation and Star Formation*. pp 151–176, doi:10.1007/978-94-009-0605-1\_12
- Schneider N., et al., 2011, *A&A*, 529, A1
- Schuller F., et al., 2017, *A&A*, 601, A124
- Soler J. D., Hennebelle P., Martin P. G., Miville-Deschênes M.-A., Netterfield C. B., Fissel L. M., 2013, *ApJ*, 774, 128
- Stutzki J., Bensch F., Heithausen A., Ossenkopf V., Zielinsky M., 1998, *A&A*, 336, 697
- Sun N.-C., et al., 2018, *ApJ*, 858, 31
- Sytine I. V., Porter D. H., Woodward P. R., Hodson S. W., Winkler K.-H., 2000, *Journal of Computational Physics*, 158, 225
- Tassis K., 2007, *MNRAS*, 382, 1317
- Teyssier R., 2002, *A&A*, 385, 337
- Wolf M., 1989, *Journal of Physics A Mathematical General*, 22, L1075
- Wu N., Li Q.-X., Zou P., 2015, *New Astron.*, 38, 1
- Xie W.-J., Jiang Z.-Q., Gu G.-F., Xiong X., Zhou W.-X., 2015, *New Journal of Physics*, 17, 103020
- de Freitas D. B., Nepomuceno M. M. F., Gomes de Souza M., Leão I. C., Das Chagas M. L., Costa A. D., Canto Martins B. L., De Medeiros J. R., 2017, *ApJ*, 843, 103
- de La Fuente Marcos R., de La Fuente Marcos C., 2006, *MNRAS*, 372, 279

## APPENDIX A: FBM IMAGES USED IN THIS ANALYSIS

The 18 fBm images generated, by varying the power-law power spectrum exponent and the random phase distribution of their Fourier transform, as reference sets for the multifractal analysis carried out in this paper are shown in Figure A1.

## APPENDIX B: EVOLUTION IN TIME OF MULTIFRACTAL PARAMETERS OF SIMULATIONS

In this appendix we expand the analysis of the MFS of numerical simulations with respect to the evolution of models with time, to assess if the trends recognised in Section 4, and in particular the broadening of the left tail of the MFS in simulations containing gravity, can be seen as genuine, or as simple fluctuations before the convergence is reached (cf., e.g., Sytine et al. 2000; Federrath et al. 2010).

For this purpose, it is necessary to follow the MFS evolution over a number of time steps larger than two. Browsing the STARFORMAT data base, one finds that the “solenoidal forcing” and “compressive forcing” scenarios are sampled with nine time snapshots (of which we analysed the second and the eighth one in the main article), while for the “quasi-hydrodynamical”, and “high-magnetization” only two time snapshots are available in all, coinciding with those analysed so far. To overcome this issue for these two simulations, on the one hand we expanded the number of analysed maps including all possible scenarios and projection directions, and on the other hand we used further simulations, as described below.

Among the geometrical features of the MFS, we here focus in particular on the width of the left tail, which can be expressed through  $\Delta\alpha_L$  (see Section 4.2.4), and on the one of the right tail ( $\Delta\alpha_R$ ), used for comparison. However, as extensively explained in Section 4, the values of  $\alpha_{10}$  and  $\alpha_{-10}$  used, respectively, to

derive those two quantities can be affected by the issue of cusp-like features in the MFS. Instead, as discussed in Section 4.3, the values of the generalised fractal dimension  $D_q$  do not suffer from this problem and, at the same time, offer a description which is completely equivalent to the one based on  $\Delta\alpha_L$  and  $\Delta\alpha_R$ . Indeed, a broadening of the left tail corresponds to a decrease of  $D_q$  at positive  $q$  orders, while for the right tail it corresponds to an increase of  $D_q$  for negative  $q$  (see, e.g., Figure 17). For this reason, we here opt for a description based on the evolution with time of the  $D_{20}$  and  $D_{-10}$  parameters (already used also in Figure 19), sensitive to large and small fluctuations in the image, respectively.

These two dimensions have been computed for all time steps available for the “solenoidal forcing” and “compressive forcing” scenarios, and are shown in Figure B1. No monotonic trend is found for both the scenarios and for both considered projections. In this respect, as already highlighted in Section 4, the  $D_{-10}$  values appear more spread than the  $D_{20}$  ones.

As said above, for the other two scenarios, only two time steps  $t_1$  and  $t_2$  are available. Thus to increase statistics, we added to our analysis the third projection direction available, namely  $xz$ , and a further “intermediate magnetization” scenario available on STARFORMAT, characterized by equal values for thermal and magnetic pressure (images can be found in the STARFORMAT web site). Figure B2 shows the evolution from  $t_1$  to  $t_2$  of the  $D_{20}$  and  $D_{-10}$  dimensions for the three scenarios, considering for each of them the three possible projections. Although based only on two time steps, this analysis shows a systematic decrease of  $D_{20}$  with time (equivalent to the broadening of the MFS left tail) for all scenarios and projection directions, explainable with the enhancement of singularities, both in number and intensity, in the maps due to the action of gravity. This is further confirmed by the fact, already suggested in Section 4, that this observed trend for  $D_{20}$  is stronger as the magnetic support of the cloud implied by the model decreases. Here, considering an additional intermediate scenario, we can further probe this hypothesis: for the “quasi-hydrodynamical” case, the slopes of the segment are -1.61, -1.38, and -1.56 for the  $xy$ ,  $yz$ , and  $xz$  projections, respectively; for the “intermediate magnetization” case, -1.36, -1.33, and -1.20; for the “high magnetization” case, -1.25, -1.02, and -1.00. Therefore, we can summarize that, within a certain degree of fluctuation due to projection effects, the MFS at large positive  $q$  shows a broadening with time due to gravity, but mitigated by the possible presence of the magnetic field. Finally, we notice an almost systematic (in eight out of nine total cases) increase of  $D_{-10}$  with time (equivalent to the broadening of the right tail of the MFS), already highlighted in Section 4. This is probably due to the appearance of small cavities in the maps as a result of the gravity action (see Figure 2, panels for time  $t_2$  of last two scenarios, especially the first of the two).

To ascertain if the observed evolution with time of the MFS can be considered genuine, one needs an analysis based on several time steps. For this reason we analysed two further sets of simulations involving gravity. The first one, obtained on purpose for this work, is based on the same approach used in Hennebelle (2018). Ten  $1024^2$  pixel column density snapshots were obtained. Only driven turbulence is present at the beginning (initial density of  $200 \text{ cm}^{-3}$ , Mach number  $\sim 10$ ), whereas gravity is switched on between the third and the fourth step. The MFS and the set of generalised fractal dimensions were computed. For the sake of brevity, here we show directly the plot of  $D_{20}$  and  $D_{-10}$  vs the time (Figure B4): while the latter do not show any particular trend with time, the former decreases after the gravity is switched on and compact structures start to appear in the maps.



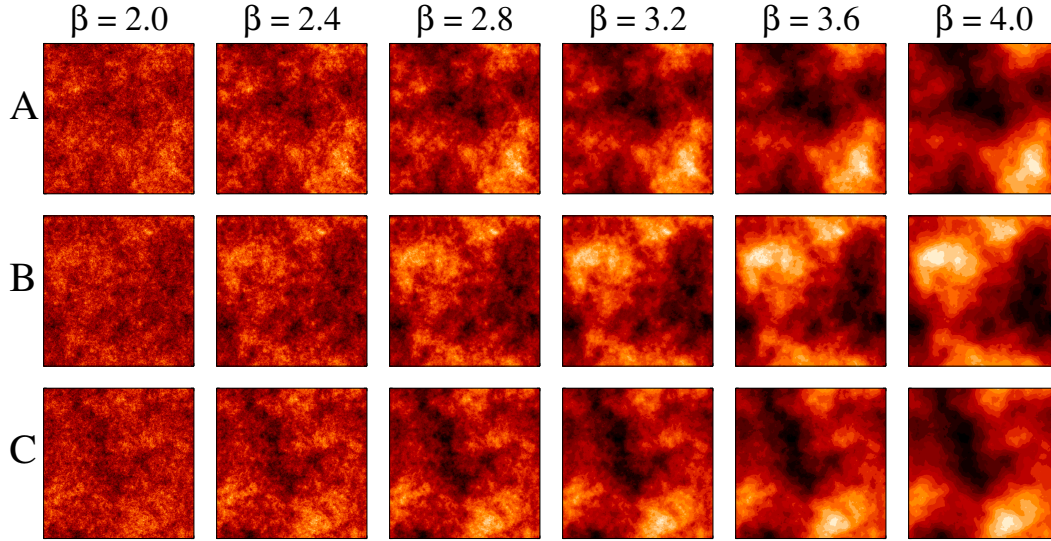


**Figure A1.** fBm  $1000 \times 1000$  pixel images generated as described in Section 2.3. Images are organized in rows according to the three different (A, B, and C) phase distributions adopted, and in columns according to the exponent  $\beta$  of their power-law power spectrum, which is reported on the top (ranging from 2 to 4 in steps of 0.4).

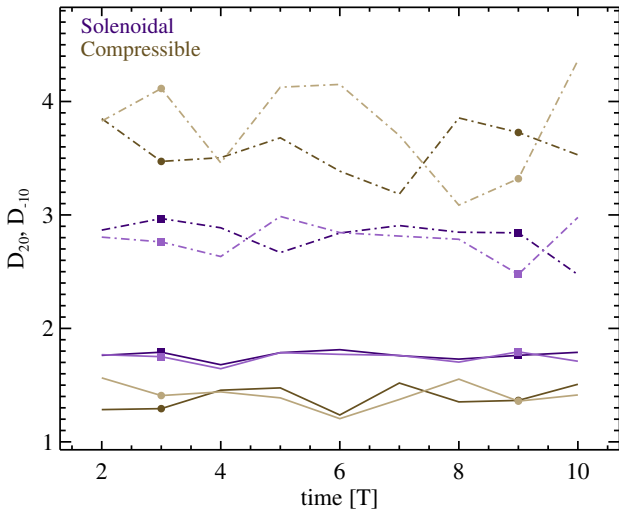


**Figure B1.** Evolution in time of the fractal dimensions  $D_{20}$  (solid lines, lower part of the plot) and  $D_{-10}$  (dotted-dashed lines, upper part) for the “solenoidal forcing” (purple) and “compressive forcing” (brown) numerical simulations of column density, respectively. The two projections  $yz$  and  $xy$  (see Section 2.2) are taken into account (darker and lighter color, respectively). The time is in units of  $\mathcal{T}$  (see Section 2.2), and the values of  $D_{20}$  and  $D_{-10}$  for  $\mathcal{T} = 3$  and 9 are marked with symbols (assigned as in Figure 8), as they coincide with those already calculated and discussed in Section 4.3.

### APPENDIX C: $\Delta$ -VARIANCE ANALYSIS OF HI-GAL FIELDS

In this work, focused on the multifractal analysis of the ISM, we also intend to compare multifractal parameters of the six investigated fields with the “classic” (mono-)fractal dimension (see Section 4.3), derived through the  $\Delta$ -variance technique (Stutzki et al. 1998), as in Paper I. However it has been necessary to repeat the  $\Delta$ -variance calculations here, both because of the addition of two new fields with respect to Paper I, namely  $\ell 215$  and  $\ell 226$ , and of the fact that, also for the other four tiles in common with Paper I, the frames

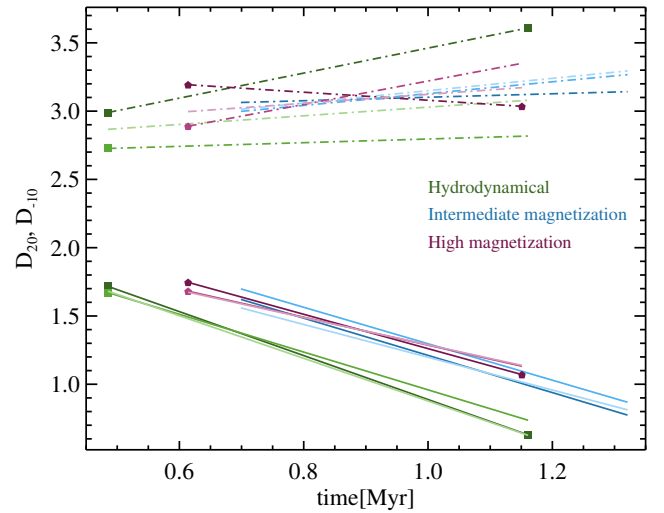


**Figure B2.** Evolution in time of the fractal dimensions  $D_{20}$  (solid lines, lower part of the plot) and  $D_{-10}$  (dotted-dashed lines, upper part) for the “quasi-hydrodynamical” (green), “intermediate magnetization” (blue), and “high magnetization” (pink) numerical simulations of column density, respectively. All three projections are taken into account (dark, intermediate and lighter color for  $yz$ ,  $xy$ , and  $xz$ , respectively). Only two time steps are available, with the two times depending on the scenario (cf. Section 2.2). As in Figure B1, the values of  $D_{20}$  and  $D_{-10}$  already calculated and shown in Section 4.3 for particular combinations of scenarios and projection directions are marked with symbols (assigned as in Figure 8).

analysed in this work are slightly different in size and position, as explained in Section 2.1.

More details, both theoretical and operational, about the  $\Delta$ -variance analysis are given in Paper I. Here we simply summarise that, in the case of a power-law power spectrum set (such as a fBm image), this technique yields a robust estimate of the exponent  $\beta$  of such spectrum without resorting to Fourier analysis. The average of the convolution of the image with a Mexican hat function with a characteristic scale length  $L$  gives the value  $\sigma_{\Delta}^2$  of the  $\Delta$ -variance

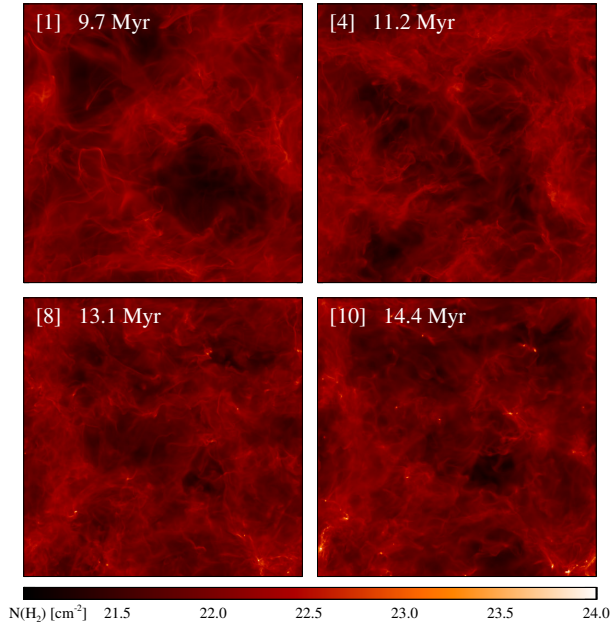


**Figure B3.** Four (out of ten) examples of column density snapshots obtained for this paper similarly to Hennebelle (2018). The number of the snapshot and the corresponding time are overwritten in white in each panel. In particular, the initial (top left) and final (bottom right) snapshots were chosen and displayed, and the first after the gravity is switched on (top right). Maps are in decimal logarithm of column density (in  $\text{cm}^{-2}$ ). The bottom color bar applies to all maps, and to improve the rendering of relatively faint structures, it saturates at a value smaller than the maximum reached in the bottom right panel, namely  $\sim 25.2$ .

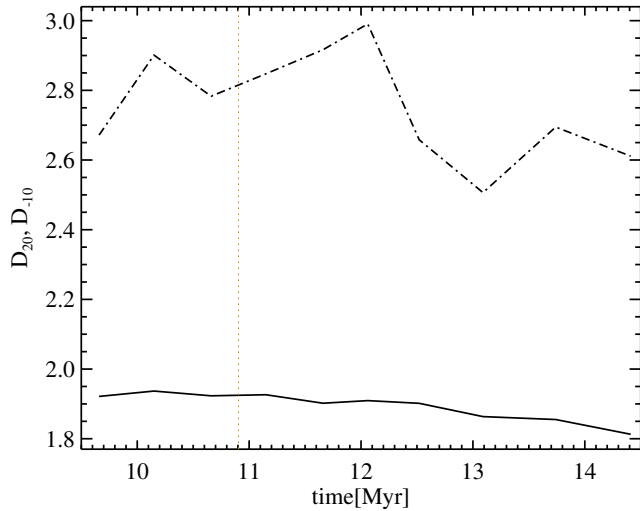


**Figure B4.** Evolution of the fractal dimensions  $D_{20}$  (solid line, lower part of the plot) and  $D_{-10}$  (dotted-dashed line, upper part) for the simulations carried out for this analysis, based on the approach of Hennebelle (2018) and partially shown in Figure B3. The dotted vertical grey line indicates the middle point between the last time step with gravity switched off and the first one with gravity switched on.

for this length. Stutzki et al. (1998) demonstrated that, for a fBm image,

$$\sigma_{\Delta}^2(L) \propto L^{2-\beta}. \quad (\text{C1})$$

A natural fractal image, instead, can exhibit such a behaviour on a limited range of scales (or on multiple ranges, with different slopes) on which it appears self-similar<sup>9</sup>.

Similarly to Paper I, in Figure C1 the  $\Delta$ -variance curves of the six Hi-GAL fields (in five bands, plus the corresponding column density maps) as a function of  $L$  are shown, with the indication of the spatial scale range identified for the determination of  $\beta$  through linear best fit of the logarithms. The fit range for the four central tiles has been kept identical to Paper I, whereas for the tiles introduced in this paper, namely  $\ell 215$  and  $\ell 226$ , it has been estimated as described in Paper I. In Table C1 the obtained values of  $\beta$ , together with the corresponding fractal dimension  $D_{\Delta}$  (according to Equation 1) are reported.

This paper has been typeset from a  $\text{T}_{\text{E}}\text{X}/\text{L}_{\text{A}}\text{T}_{\text{E}}\text{X}$  file prepared by the author.

<sup>9</sup> As in Paper I, here for each tile we identify an appropriate range on which all wavelengths show an approximately power-law behaviour.

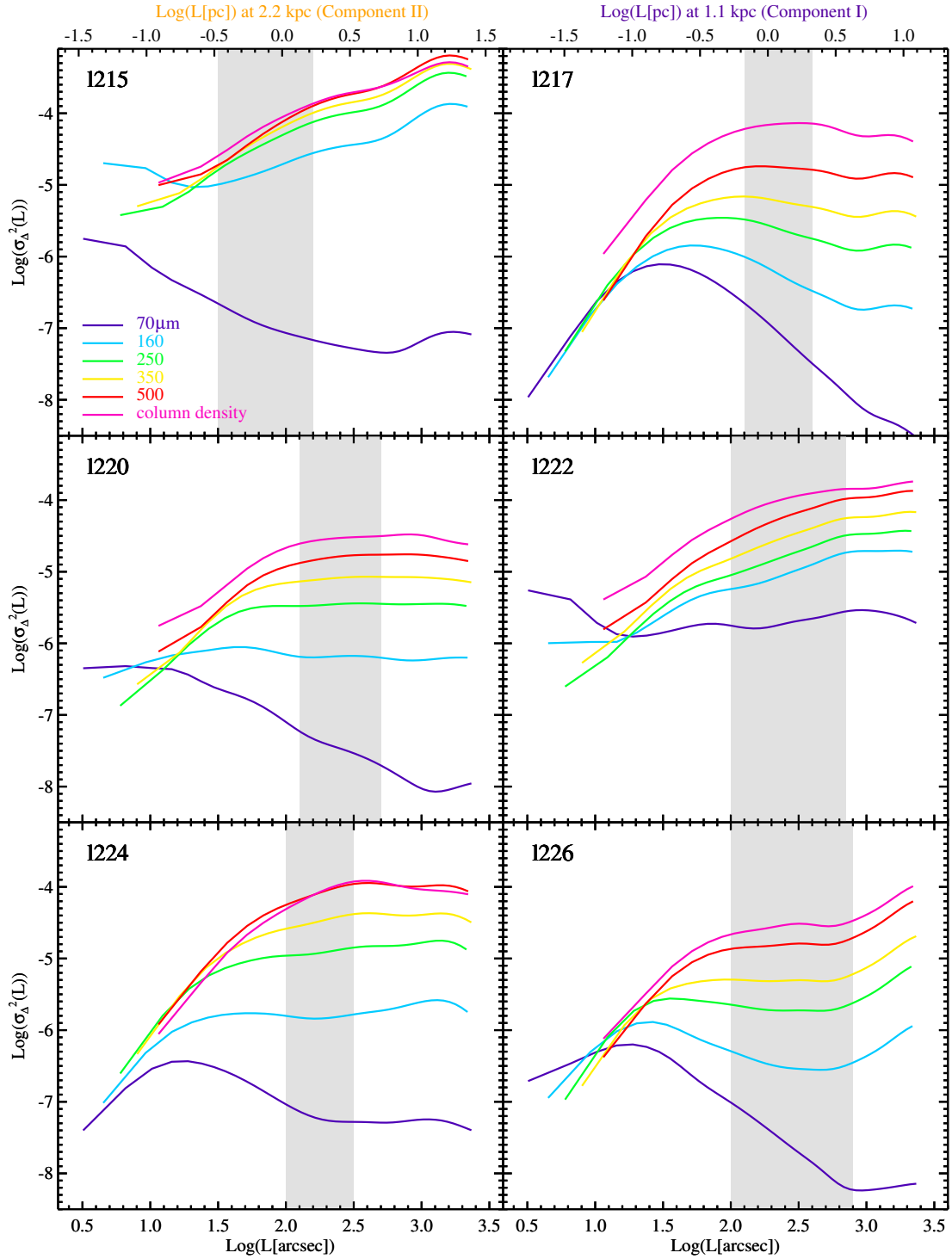


**Figure C1.**  $\Delta$ -variance curves of the maps shown in Figure 1 using the same tile naming and band-color encoding (this figure is similar to Figure 4 of Paper I). Tiles associated to velocity component II are in the left panels, those associated with component I are in the right panels (for reference, the spatial scales corresponding to angular scales at the distances of the two components are reported on the top axis of the two upper panels, respectively). We use the same axis ranges in all panels to allow a direct comparison of the slopes. The inertial range is highlighted as a grey area in each panel. The corresponding linear slopes are transformed in power spectrum slopes (see text) are reported in Table C1.

**Table C1.** Power spectrum exponent and fractal dimension of the investigated Hi-GAL maps

Field	Distance [kpc]	Fit range [pc]	$\beta$					$D$				
			160 $\mu\text{m}$	250 $\mu\text{m}$	350 $\mu\text{m}$	500 $\mu\text{m}$	Col. dens.	160 $\mu\text{m}$	250 $\mu\text{m}$	350 $\mu\text{m}$	500 $\mu\text{m}$	Col. dens.
$\ell$ 215	2.2	0.3–1.7	2.65	2.94	3.05	3.21	3.02	2.67	2.53	2.47	2.40	2.49
$\ell$ 217	2.2	1.3–4.2	0.99	1.44	1.67	1.92	2.17	3.50	3.28	3.17	3.04	2.92
$\ell$ 220	2.2	1.3–5.3	2.03	2.07	2.11	2.20	2.16	2.99	2.97	2.95	2.90	2.92
$\ell$ 222	1.1	0.5–3.8	2.65	2.67	2.68	2.69	2.47	2.67	2.66	2.66	2.66	2.76
$\ell$ 224	1.1	0.5–1.7	2.05	2.25	2.43	2.62	2.82	2.97	2.87	2.78	2.69	2.59
$\ell$ 226	1.1	0.5–4.2	1.81	1.99	2.02	2.10	2.14	3.09	3.00	2.99	2.95	2.93